The Astrophysical Journal, 729:129 (21pp), 2011 March 10 doi:10.1088/0004-637X/729/2/129

GALAXY KINEMATICS WITH VIRUS-P: THE DARK MATTER HALO OF M87

Jeremy D. Murphy, Karl Gebhardt, and Joshua J. Adams
Department of Astronomy, University of Texas at Austin, 1 University Station C1400, Austin, TX 78712, USA; murphy@astro.as.utexas.edu
Received 2010 October 11; accepted 2011 January 2; published 2011 February 17

ABSTRACT

We present two-dimensional stellar kinematics of M87 out to $R = 238''$ taken with the integral field spectrograph VIRUS-P. We run a large set of axisymmetric, orbit-based dynamical models and find clear evidence for a massive dark matter halo. While a logarithmic parameterization for the dark matter halo is preferred, we do not constrain the dark matter scale radius for a Navarro–Frenk–White (NFW) profile and therefore cannot rule it out. Our best-fit logarithmic models return an enclosed dark matter fraction of $17.2^{+5.0}_{-5.0}$% within one effective radius ($R_e \cong 100''$), rising to $49.4^{+7.2}_{-8.8}$% within 2 R_e. Existing SAURON data ($R \leqslant 13''$), and globular cluster (GC) kinematic data covering $145'' \leqslant R \leqslant 554''$ complete the kinematic coverage to $R = 47$ kpc ($\sim 5\ R_e$). At this radial distance, the logarithmic dark halo comprises $85.3^{+2.5}_{-2.4}$% of the total enclosed mass of $5.7^{+1.3}_{-0.9} \times 10^{12}\ M_\odot$ making M87 one of the most massive galaxies in the local universe. Our best-fit logarithmic dynamical models return a stellar mass-to-light ratio (M/L) of $9.1^{+0.2}_{-0.2}$ (V band), a dark halo circular velocity of 800^{+75}_{-25} km s^{-1}, and a dark halo scale radius of 36^{+7}_{-3} kpc. The stellar M/L, assuming an NFW dark halo, is well constrained to $8.20^{+0.05}_{-0.10}$ (V band). The stars in M87 are found to be radially anisotropic out to $R \cong 0.5\ R_e$, then isotropic or slightly tangentially anisotropic to our last stellar data point at $R = 2.4\ R_e$ where the anisotropy of the stars and GCs are in excellent agreement. The GCs then become radially anisotropic in the last two modeling bins at $R = 3.4\ R_e$ and $R = 4.8\ R_e$. As one of the most massive galaxies in the local universe, constraints on both the mass distribution of M87 and anisotropy of its kinematic components strongly inform our theories of early-type galaxy formation and evolution in dense environments.

Key words: dark matter – galaxies: elliptical and lenticular, cD – galaxies: kinematics and dynamics

Online-only material: color figures

1. INTRODUCTION

Dark matter is a central component of our current theory of large-scale structure formation. Although the nature of dark matter is unknown, significant support for this cosmological paradigm comes from well-motivated physical arguments (Gunn & Gott 1972; Press & Schechter 1974; White & Rees 1978; Fillmore & Goldreich 1984) and the remarkable agreement between N-body simulations of the growth of structure (Frenk et al. 1985; Davis et al. 1985; Navarro et al. 1995; Springel et al. 2005) and observations of the distribution of galaxies in the local universe (Davis et al. 1982; Colless et al. 2001).

With the increase in computational power seen over the past 30 years, the spatial resolution of numerical simulations has improved to the point where individual galaxies are well resolved and their dark matter halos can be studied in detail (Moore et al. 1998a; Ghigna et al. 2000; Springel et al. 2008; Boylan-Kolchin et al. 2009). From the study of both cosmological and galaxy scale simulations, different parameterizations for a universal dark matter density profile have emerged. Einasto introduced an early parameterization (Einasto 1965, 1968) based on the Sérsic profile for the light distribution in galaxies (Sersic 1968). Other dark matter profile parameterizations have followed (Dubinski & Carlberg 1991; Navarro et al. 1997; Moore et al. 1998b). While each parameterization has found some level of success at describing the distribution of mass on the scales of galaxy clusters, understanding the extent and shape of galaxy-sized dark matter halos has met with mixed success.

Observationally, the study of dark matter halos in spiral galaxies has outpaced that of ellipticals. This is largely due to the presence of extended H I disks found in spiral galaxies which provide a clean dynamical tracer to several effective radii (Rubin et al. 1980; van Albada & Sancisi 1986; Jimenez et al. 2003). Analysis of the circular velocity curves of spiral galaxies provides some of the strongest evidence for the existence of dark matter on galaxy scales (see Sofue & Rubin 2001 for a review). Lacking the extended H I disks seen in spiral galaxies, progress toward constraining the extent and distribution of dark matter in elliptical galaxies has proven a greater challenge. Despite this complication, evidence from gravitational lensing (Keeton 2001; Mandelbaum et al. 2006; Sand et al. 2008; Carrasco et al. 2010), X-ray gas profiles (Humphrey et al. 2006; Churazov et al. 2008; Das et al. 2010), planetary nebulae (PNe) and globular cluster (GC) kinematics (Côté et al. 2001; Douglas et al. 2007; Coccato et al. 2009), and integrated light stellar kinematics (Bender et al. 1994; Emsellem et al. 2004; Cappellari et al. 2006; Thomas et al. 2007; Weijmans et al. 2009; Forestell 2009) has shown that elliptical galaxies are typically dark matter dominated beyond $R \sim 1.5\ R_e$. However, not all galaxies studied show definitive evidence for the existence of dark matter (Gerhard et al. 2001; Romanowsky et al. 2003; Moni Bidin et al. 2010) and the best choice of dark halo parameterization remains elusive. These open questions leave key components of our theories of the growth of structure, galaxy formation, and evolution largely in the dark.

Comparison between the results of various mass estimation methods returns agreement for certain systems and disagreement for others. Coccato et al. (2009) find good agreement between integrated stellar light absorption line kinematics and PNe data for a sample of 16 early-type galaxies. Yet in other systems the agreement is poor. In an analysis of NGC1407, the central elliptical galaxy in a nearby evolved galaxy group, Romanowsky et al. (2009) find a discrepancy between the mass profile determined from GC kinematics and the profile determined by X-ray gas. For the brightest cluster galaxy in A3827,

Carrasco et al. (2010) determine an enclosed mass via strong lensing that is 10× higher than the mass determined from X-ray measurements. Mass discrepancies extend to tracers other than X-ray gas. Stellar kinematics of NGC821 from Forestell & Gebhardt (2010) and NGC3379 from Weijmans et al. (2009) disagree with the PNe measurements of Romanowsky et al. (2003).

Each of these methods for estimating mass brings its own set of advantages, assumptions, and limitations. Mass estimates based on X-ray gas have the advantage of very extended coverage, providing spatial overlap between the other methods. Yet X-ray gas analysis is limited to massive galaxies and commonly assumes hydrostatic equilibrium of the gas. Strong lensing mass estimates avoid this potential pitfall as it makes no assumptions regarding the energy distribution of the material within the lens. However, lensing is limited in its flexibility, as the regions of the universe available for exploration are dictated by the fixed geometry of the lens and source. Velocity dispersion measurements from integrated stellar light are effectively available for all local systems, but require a parameterization of the dark halo and involve assumptions about the degree of triaxiality of the system. There is also the challenge of getting stellar kinematics at large radii where the dark halo comes to dominate the mass. PNe and GCs have an advantage here as they typically extend to large radii, yet whether these tracers follow the same dynamical history, and therefore probe the same formation history as the stars, is not clear for all systems. A natural approach is to combine various data sets and methods in order to apply the strengths of one method to overcome the shortcomings of another. Treu & Koopmans (2004) and Bolton et al. (2008) take this approach with good success by using both lensing and stellar kinematics to break the well-known mass–anisotropy degeneracy (Dejonghe & Merritt 1992; Gerhard 1993).

We focus here on the dark matter distribution in the giant elliptical galaxy M87, the second-rank galaxy in the Virgo Cluster. M87 has been extensively studied and a number of groups have made estimates of the extent of M87's mass profile with a variety of methods. Empirical formulae, based on the virial theorem and measurements of the central stellar velocity dispersion, returned some of the earliest mass estimates for M87 (Poveda 1961; Brandt & Roosen 1969; Nieto & Monnet 1984). Sargent et al. (1978) used stellar velocity dispersion measurements extending to $R \sim 0.7\,R_e$ and the photometry of Young et al. (1978) to calculate the mass-to-light ratio (M/L) as a function of radius and estimate enclosed mass. Since that time, other mass estimates of M87 using X-ray gas (Fabricant & Gorenstein 1983; Tsai 1996; Matsushita et al. 2002; Das et al. 2010) and GC kinematics (Huchra & Brodie 1987; Mould et al. 1987; Merritt & Tremblay 1993) have been made. A comparison of these values to the mass estimate made in this work is given in Section 5.2.

The outline of the paper is as follows. In Section 2, we give the details of the data sets used in our dynamical modeling, with specifics on the Visible Integral-field Replicable Unit Spectrograph-Prototype (VIRUS-P) instrument given in Section 2.4. An overview of the data reduction steps is given in Section 3, with the complete details provided in the Appendix. Section 3.1 explains the extraction of the line-of-sight velocity dispersion profile (LOSVD) and Section 3.3 provides details of the selection of template stars and their application. In Section 4, we explain the orbit-based dynamical models. In Section 5, we give the results of our dynamical modeling, with a discussion of our enclosed mass estimates and a comparison of the logarithmic and Navarro–Frenk–White (NFW) halos found in Sections 5.1 and 5.2. We explore possible systematics in Section 5.4.

We assume a distance to M87 of 17.9 Mpc, corresponding to a scale of 86.5 pc arcsec^{-1}.

2. DATA

We make use of three sets of kinematic data to dynamically model M87. At large radii ($140'' \leqslant R \leqslant 540''$), we use GC kinematics (Côté et al. 2001). Stellar kinematics from the SAURON data set (Emsellem et al. 2004) are used within the central 13″. New stellar kinematics, taken with VIRUS-P (Hill et al. 2008b), cover $4'' \leqslant R \leqslant 238''$ and add substantially to the two-dimensional spatial coverage of the galaxy. We provide details of the stellar surface brightness and GC data in Section 2.1. The SAURON stellar kinematics are discussed in Section 2.2. In Section 2.3, we describe the observations made with VIRUS-P. Section 2.4 gives details of the VIRUS-P spectrograph and Section 2.5 explains the data collection.

2.1. Photometry and Globular Cluster Kinematics

The application of both the stellar surface brightness profile and GC data follows Gebhardt & Thomas (2009, hereafter GT09). The *V*-band photometry comes from Kormendy et al. (2009), which is a combination of *Hubble Space Telescope* (*HST*) data from Lauer et al. (1992) and various ground-based observations. This photometry extends from 0.″02 to 2200″. As the dynamical modeling requires the stellar surface density, the surface brightness profile is deprojected following the method of Magorrian (1999). Our GC surface density profile comes from McLaughlin (1999) and is deprojected via a non-parametric spherical inversion as described in Gebhardt et al. (1996). The GC velocities are reported in Cohen & Ryzhov (1997), Cohen (2000), and Hanes et al. (2001) and compiled in Côté et al. (2001). We employ the same cuts to remove foreground and background contamination as described in Côté et al. (2001). These cuts leave us with 278 GC velocities which we divide into 11 modeling bins. An LOSVD is then determined from all GCs within one modeling bin as described in GT09.

2.2. SAURON Stellar Kinematics

The SAURON data set provides two-dimensional spatial coverage of M87 out to nearly 40″ with superior spatial resolution to VIRUS-P. We therefore use SAURON kinematics in the central region of M87. Once the size of the modeling bins makes the SAURON spatial resolution irrelevant ($R \geqslant 8''$) the VIRUS-P data are used. We elect to use both SAURON and VIRUS-P kinematics between $8'' \leqslant R \leqslant 13''$ as described in Section 4.2.

The publicly available SAURON kinematics are parameterized by the first four coefficients of a Gauss–Hermite polynomial expansion. As our dynamical modeling fits the full LOSVD rather than its moments, we reconstruct the LOSVD via Monte Carlo simulations based on the errors provided by SAURON. The details of this reconstruction can be found in GT09.

2.3. VIRUS-P Stellar Kinematics

The VIRUS-P data were taken during three separate observing runs over 10 partial nights in 2008 January, 2008 February, and 2009 February. VIRUS-P has no dedicated sky fibers. Therefore, sky nods are necessary and constitute approximately one-third of our observing time. All our VIRUS-P data for

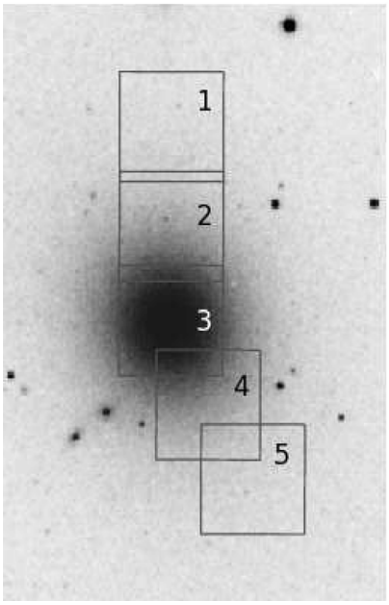

Figure 1. SDSS image of M87 showing the positions of the five VIRUS-P pointings. Each 107″ × 107″ box consists of a hexagonal array of 246 optical fibers (see Figure 2). The total exposure time for each pointing is given in Table 1. North is up and east is to the right.

Table 1
Exposure Times for M87 Pointings

Pointing	Exposure Time (minutes)	Observation Date	R_{min} (″)	R_{max} (″)
1	180	01–08	130.0	238.0
1	120	02–08	130.0	238.0
2	100	01–08	45.0	140.0
3	60	02–09	0.0	73.0
4	120	02–08	43.0	136.0
5	240	02–08	127.0	203.0

Notes. The exposure times, date of observation, and radial positions of the five VIRUS-P pointings on M87. The exposure times quoted are the total science exposures included in the final VIRUS-P data. Ten of the 51 exposures taken were withheld from the reductions based on analysis of the S/N of the resulting spectra. Sky nod exposure time is not included in these totals. All observing conditions were good to photometric, with typical seeing values of 1.″5. These data were all taken within ±3 days of the new moon.

M87 were acquired through a cadence of 20 minute science exposures bracketed by 5 minute sky nods. We note that while not having dedicated sky fibers presents issues with determining the correct level of sky subtraction, sampling the sky with all 246 fibers allows us to better match the point-spread function (PSF) variation from fiber to fiber while not adding substantially to our photon noise. A discussion of both the advantages and drawbacks of sky nods, and the details of our sky subtraction method are given in Appendix A.2.

The VIRUS-P data for M87 consist of five pointings extending to 238.″0 (20.6 kpc). The pointing placements are shown in Figure 1 with the relative size and positions of the fibers on-sky shown in Figure 2. Exposure times and radial distances for each pointing are given in Table 1. Ten of the 51 science exposures were taken under marginal conditions and withheld from the final data set as they degraded our signal-to-noise ratio (S/N). The exposure times quoted in Table 1 include only the data that went into the final spectra and subsequent modeling.

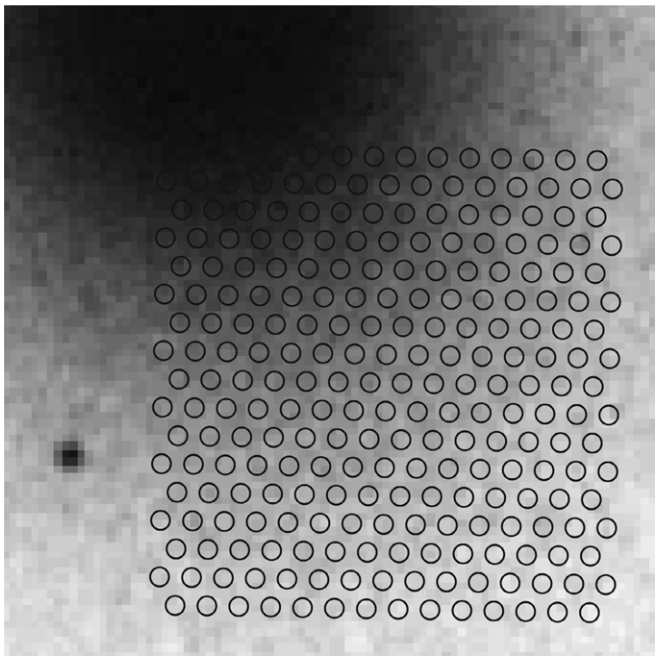

Figure 2. Relative positions of the 246 fibers comprising pointing 4. The fibers are aligned in a hexagonal array with a one-third fill factor. Each fiber has a 4.″1 on-sky diameter.

2.4. The VIRUS-P Instrument

The VIRUS-P, currently deployed on the Harlan J. Smith 2.7 m telescope at McDonald Observatory (Hill et al. 2008b), is a prototype for the VIRUS instrument (Hill et al. 2006). VIRUS is a replicated, fiber fed spectrograph currently under development for the Hobby Eberly Telescope Dark Energy eXperiment (HETDEX; Hill et al. 2008a). Originally designed to conduct an Lyα emitter survey (Adams et al. 2011; Blanc et al. 2010), the VIRUS-P spectrograph is proving an excellent stand-alone instrument for a wide range of scientific problems (Adams et al. 2009; Blanc et al. 2009; Yoachim et al. 2009, 2010). VIRUS-P is a gimbal-mounted integral field unit spectrograph composed of 246 optical fibers each with a 4.″1 on-sky diameter. The CCD is a 2048 × 2048 back-illuminated Fairchild 3041 detector. The wavelength range for these observations is 3545–5845 Å. The fibers are laid out in an hexagonal array, similar to Densepak (Barden & Wade 1988), with a one-third fill factor and a large (107″ × 107″) field of view. The large fibers and field of view make VIRUS-P an extremely efficient spectrograph for observing extended, low surface brightness objects such as the faint outer halos of elliptical galaxies. Gimbal-mounted directly to the barrel of the telescope, VIRUS-P maintains a constant gravity vector. Extensive analysis of the fiber-to-fiber wavelength solution and fiber spatial PSF has been conducted and shows negligible evolution over a night. To quantify the evolution, the location of the centers of the fibers from the twilight flats taken at the start and end of the night is compared and found to deviate $\leqslant$0.1 pixels for all nights. The wavelength solution determined from the arc lamps taken at dusk and dawn is also compared. Typical residuals of the wavelength solution to known arc lines show an rms scatter of ∼0.05 Å for frames taken at the same time of night. This value of rms scatter does not increase when arcs from both dusk and dawn are combined. The one exception occurs with large temperature swings ($\geqslant$10°C). Thermal contraction or expansion of the input and output ends of the fiber bundle can lead

to a change in position and stress pattern on individual fibers. Localized pressure on a fiber can lead to focal ratio degradation (Craig et al. 1988; Schmoll et al. 2003) resulting in changes to the fiber position and spatial PSF over a night and increased rms scatter in the wavelength solution residuals. These effects are subtle, yet can degrade the quality of our flat fielding. Therefore, if a temperature change $\geqslant 10^{\circ}$ C is seen over a night, the data are split into two groups and reduced using the calibration frames taken at the closest temperature. We found this approach was necessary for two nights in our 2009 January observing run. However, even when a steep temperature gradient is seen, wavelength and flat-field calibration frames are necessary only at the start and end of a night's observing.

The median spectral resolution for this VIRUS-P data is 4.75 Å FWHM as determined from Gaussian fits to strong emission lines in the arc lamp frames. This resolution corresponds to an instrumental dispersion (sigma) of $\sim$150 km s^{-1} at 4060 Å and $\sim$112 km s^{-1} at 5400 Å. VIRUS-P was refocused between our 2008 January/February and 2009 February observing runs which led to a non-trivial change (ΔFWHM $\simeq$ 0.5 Å) in the instrumental resolution. As we frequently combine the spectra from different fibers and different nights, the change in instrumental resolution is taken into account when extracting the stellar LOSVDs. The details of how differences in instrumental resolution are handled can be found in Section 3.3.

The assumption of a Gaussian spectral PSF for VIRUS-P proves to be a good one. To quantify this, we fit Gauss–Hermite coefficients to four bright lines in our mercury–cadmium arc lamp frames for all 246 fibers. Over the four spectral lines and all fibers the median H3 coefficient is 0.003 ± 0.013. The median H4 coefficient is 0.0003 ± 0.0117. Any non-Gaussian line behavior is further mitigated by the high dispersion of M87, which puts us well above the instrumental resolution.

2.5. Data Collection

Calibration frames, taken at the start and end of each observing night, consist of a set of twilight frames, mercury and cadmium arc lamp frames, and bias frames. The twilight frames are used for both flat fielding and determining the position and shape of each fiber profile. The arc lamp frames are used for the wavelength solution and determination of the instrumental resolution (see Appendix A.1 for more details). The remainder of an observing night involves a sequence of 5 minute sky nods and 20 minute science frames. The sky nods were taken 30′ off the galaxy center in a region of sky with minimal field stars and continuum sources and where the galaxy has a surface brightness of $\mu_b \sim 26.5$ (Kormendy et al. 2009). While this position still includes intracluster light known to extend across much of the core of the Virgo Cluster (Mihos et al. 2005), the contribution to the total flux is very low.

3. DATA REDUCTION OVERVIEW

We provide a brief overview of the data reduction process here, up through extraction of the kinematics. The extensive details can be found in the Appendix.

The primary data reduction steps are completed with Vaccine, an in-house data reduction pipeline developed for VIRUS-P data. The reduction steps are as follows. All of the science, sky and calibration frames are overscan-subtracted. A master bias is created by combining all the overscan-subtracted bias frames taken during an observing run. The arcs and twilight flats are then combined using the biweight estimator (Beers et al. 1990). A fourth-order polynomial is fit to the peaks of each of the 246 fibers for each night. We refer to this as the fiber *trace*. This polynomial fit is then used on each science and sky frame to extract the spectra, fiber by fiber, within a 5 pixel-wide aperture centered around the trace of the fiber. The wavelength solution is determined for each fiber, and for each night, based on a fourth-order polynomial fit to the centers of known mercury and cadmium arc lamp lines. The twilight flats are normalized to remove the solar spectra. These normalized flats are then used to flatten the science and sky data. Once the frames are flattened, the neighboring sky frames are appropriately scaled, combined, and subtracted from the science frames. Cosmic rays are located and masked from each 20 minute science frame. For the dynamical modeling, the galaxy is divided into a series of line-of-sight radial and angular spatial bins. Therefore, fibers that fall within a spatial bin are combined. This step leaves us with individual spectra for 88 different spatial bins. Of these 88 spectra, the eight central spectra are withheld from the dynamical modeling, as the SAURON data have superior spatial resolution in the central region. The next step before the data are ready to model is the determination of the LOSVD, described below.

3.1. Extraction of the LOSVD

Our method for determination of the LOSVD follows Gebhardt et al. (2000) and Pinkney et al. (2003). We give an overview of the method here.

To begin, an initial guess for a non-parametric LOSVD of the stars is made. This LOSVD is distributed into 29 velocity bins and then convolved with a set of 12 template stars taken from the Indo-US template library. Selection of the template stars is discussed in Section 3.3. The continuum is divided out of both galaxy and template spectra prior to fitting. The fitting routine works by allowing both the weights given to each of the 29 velocity bins and the weights given to each template star to vary. A parameter to allow for an adjustment to the overall continuum of the template stars is also allowed to float. Minimization of the residuals of the fit of the convolved stellar template spectra to the galaxy spectra is used to determine the best LOSVD for that given spatial bin and spectral region.

One of the great advantages VIRUS-P provides in the extraction of the LOSVD and subsequent error estimates is its wide wavelength range ($\sim$2200 Å). The wide wavelength coverage allows us to determine the best LOSVD in five different wavelength regions. Of the five spectral regions sampled (Table 2), four of the spectral regions are used in the final modeling. The Ca H + K spectral region (3650–4150 Å) proves difficult to fit and exhibits a large systematic offset in all of the first four moments of the LOSVD from the other four spectral regions, likely due to issues with the continuum division. This region is therefore not included in the determination of the final LOSVD and error estimate.[1] The final LOSVD is created by taking the average of the four LOSVDs within each of the 29 velocity bins. Figure 3 shows two of the final 88 LOSVDs, with errors, for a bin at $R = 24''$ and $R = 174''$. Overplotted in these figures are the LOSVDs from the four spectral regions used to generate the final LOSVDs.

[1] Since the completion of the dynamical modeling, the continuum normalization issue experienced with the Ca H + K region has been solved. However, this region is not included in the dynamical models as the cost of re-running 1000s of models is prohibitive. We note Figure 5 where the Ca H + K region is included in the analysis of the systematic offset seen in the Mg *b* spectral region.

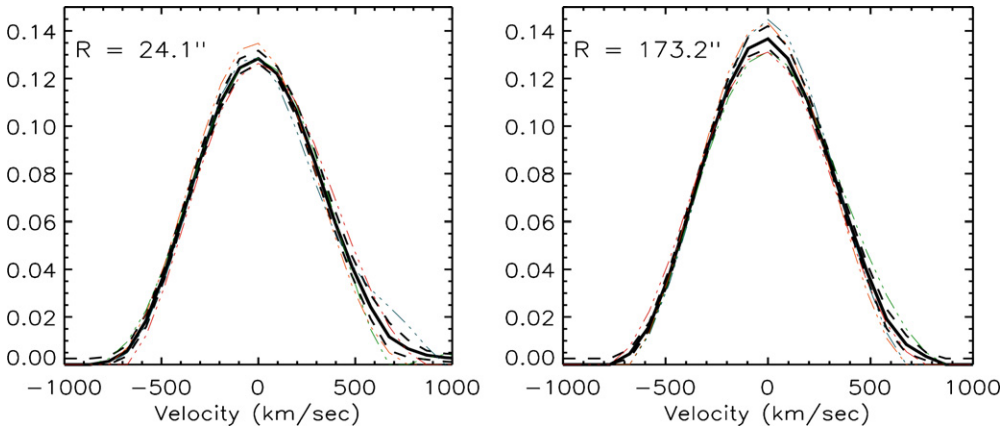

Figure 3. Two LOSVDs from spatial bins at $R = 24\farcs1$ (left) and $R = 173\farcs2$ (right), plotted with their uncertainties. Overplotted with lighter colored lines are the LOSVDs from the four wavelength regions used to determine the final LOSVD. Seventy-nine of the 80 final modeling LOSVDs are constructed from four of the LOSVDs determined from the four spectral regions shown in Table 2. For one spatial bin, the iron region (5300–5850 Å) proved a poor fit and was withheld from the final LOSVD.

(A color version of this figure is available in the online journal.)

Table 2
VIRUS-P Spectral Regions

Wavelength Range (Å)	Spectral Features
3650–4050	Ca H, Ca K
4195–4585	*G* band
4455–4945	H-beta
4930–5545	Mg I b
5300–5850	Iron

Notes. The five spectral regions chosen for extraction of the best-fit LOSVD for each spatial bin. The calcium H and K region (3650–4050 Å) is not used in the determination of the final LOSVD due to a systematic offset in the measured velocity dispersion as compared to the other spectral regions. This systematic is likely due to issues with the continuum normalization over the blue region of the spectra (see Footnote 1 and Section 3.5 for further discussion).

A smaller systematic offset was observed for the Mg *b* spectral region (see Figures 5 and 6). Yet unlike the Ca H + K offset, which stems from the difficulty in determining the placement of blue continuum, we believe this offset is inherent to the Mg *b* spectral region and therefore elect to include it in our final LOSVDs and subsequent modeling. This decision was made as a tradeoff between the ∼10% offset in velocity dispersion seen with this spectral region, and the mitigating effects a fourth spectral region has on the statistics of the final LOSVD and uncertainty estimates. We note also that by including the Mg *b* spectral region, our claim of a massive dark matter halo is strengthened as the direction for the Mg *b* offset is toward lower velocity dispersions. We pick up this discussion in Section 3.5.

3.2. Uncertainty Estimates

Error estimates for the best-fit LOSVD for each spatial bin are determined in two ways. The first is made via Monte Carlo simulations while the second is an empirical method that makes use of the wide wavelength coverage of VIRUS-P. Then, for each velocity bin in each LOSVD, the largest of the uncertainties is taken as the uncertainty for that velocity bin. Both methods are described here.

The first error estimate is made by a Monte Carlo bootstrap method for each of the four spectral regions used in the final LOSVD. The best-fit convolved LOSVD and set of weighted template stars provide the starting point for 100 Monte Carlo realizations. Each realization involves a randomly chosen flux value, drawn from a Gaussian distribution, for each wavelength. The mean of the Gaussian distribution is the flux from the best-fit convolved template spectra, and the standard deviation is set as the mean of the pixel noise values for that spatial bin as determined in the Vaccine reductions. A new LOSVD is determined for all 100 realizations and provides a distribution of values for all 29 velocity bins in the best-fit LOSVD. The error estimate is the standard deviation of the 100 realizations within each of the 29 velocity bins. This Monte Carlo simulation is run on all four spectral regions and returns four error estimates for each of the 29 velocity bins in each of the 88 spatial bins.

The second method for estimating the uncertainty is made by calculating the standard deviation of the four LOSVDs within each of the 29 velocity bins. This error estimate, combined with the four from the Monte Carlo simulations, gives us five estimates of the uncertainty within each of the 29 velocity bins of the LOSVD. The largest uncertainty at each of these steps is taken as the final uncertainty used in the dynamical modeling. We note that both the Monte Carlo and empirical methods for determining the uncertainty return similar results, with the empirical method typically being larger.

3.3. Stellar Template Library

The template stars used in the extraction of the LOSVD come from the Indo-US spectral library (Valdes et al. 2004). The 12 stars in our final template library (Table 3) were chosen from an initial list of 40 stars selected to cover a range in stellar type and metallicity. These 12 stars were selected from the initial list as they returned the lowest residuals when fit to the spectra while still maintaining a good range in stellar type. As the resolution of the template stars does not match the instrumental resolution of VIRUS-P, we must convolve the template stars with the instrumental resolution of VIRUS-P. The instrumental resolution varies both between fibers and, as the instrument was refocused in 2009 April, between observing runs. A further complication is that spectra from several fibers are often combined to reach the desired S/N. For overlapping pointings, this combination can involve spectra from opposite ends of the CCD where the instrumental resolution can be

Table 3
Indo-US Template Stars

ID	Type	V	[Fe/H]
HD 50420	A7III	6.16	0.30
HD 78362	F5III	4.65	0.52
HD 5015	F8V	4.82	0.00
HD 693	F5V	4.89	−0.38
HD 39833	G0III	7.66	0.04
HD 161797	G5IV	3.41	0.16
HD 199960	G1V	6.21	0.11
HD 17820	G5V	8.38	−0.69
HD 20893	K3III	5.09	−0.13
HD 6734	K0IV	6.46	−0.25
HD 92588	K1IV	6.26	−0.10
HD 130025	K0V	6.16	−0.19

Notes. The template stars used in the determination of the best-fit LOSVD. These 12 stars were selected from an initial list of 40 stars based on a minimization of the fitting residuals during the kinematic extraction.

different by as much as 0.7 Å FWHM. For a galaxy like M87, with velocity dispersions around 300 km s^{-1}, the error introduced by ignoring this difference is small (∼2%). A simple solution, particularly given M87's high velocity dispersion, would be to convolve all the spectra to the lowest instrumental resolution. However, as we are interested in developing data reduction methods to accept all of the galaxies in our sample, we avoid degrading our resolution to the lowest value in the following manner.

The instrumental resolution is calculated from Gaussian fits to eight unblended arc lines from the arc lamp calibration frames taken each night. As the instrumental resolution values are noisy, particularly at weaker spectral lines, a small, smoothing boxcar (five fibers wide) is run along the spatial direction. Measurements of the focal ratio degradation of the VIRUS-P fibers show minimal fiber-to-fiber variation (⩽2%; Murphy et al. 2008). As focal ratio degradation is the dominant characteristic of an optical fiber impacting instrumental resolution, differences in the instrumental resolution across the spatial direction of the chip are due to optical effects *after* the light exits the fiber. As resolution changes stemming from optical effects should be continuous, a boxcar smoothing of the instrumental resolution values is justified. Differences in the calculated instrumental resolution from night to night over an observing run are ∼1% and so one instrumental resolution map is made for an entire observing run. The worst instrumental resolution over our data set is 5.0 Å FWHM at 4060 Å and 4.4 Å FWHM at 5673 Å. Once an estimate of the instrumental resolution for every fiber and for each observing run is made, the instrumental resolution for each fiber going into a spatial modeling bin receives a normalized weight based on the number of exposures going into the final spectra. This approach gives more weight to fibers that provide more weight to the final spectra while accounting for differences in instrumental resolution between fibers and observing runs. Due to M87's high velocity dispersion, this step amounts to a negligible change in the final LOSVD.

Initially, we explored using template stars taken with VIRUS-P to avoid the complications of convolving the template spectra with the instrumental resolution. The results achieved by this method proved less robust for two primary reasons. First, the S/N of the Indo-US spectra is very high. While it is certainly possible to reach this S/N with VIRUS-P, there are observing time costs to consider. As using template stars taken with the instrument is effective only if we are able to fully sample the instrumental resolution across the CCD, many exposures on the same template star are necessary. The second limitation is the variety of stellar types available during an observing run. Although some variety in stellar type and metallicity is achievable, significant observing time would be lost in attempting to build up a sufficiently diverse stellar library.

3.4. Moments of the LOSVDs

In Figure 4, we plot the first four Gauss–Hermite moments of the LOSVDs from each of our 88 spatial bins. The colored diamonds indicate the angular position on the galaxy, with black along the major axis followed by blue, green, orange, and red falling along the minor axis. For visual clarity, error bars are plotted only for data along the major axis. The error bars along the other axes are of comparable size. The vertical dashed lines indicate where the SAURON kinematics are used over the VIRUS-P data in the dynamical modeling. Overplotted with open diamonds are moments from the best-fit logarithmic model at each spatial bin, after averaging over the angular bins. To minimize visual confusion, the model fits have not been plotted in the central region.

3.5. Systematics in Stellar Kinematics

We have found a systematic offset between our measurement of velocity dispersion when compared to the SAURON data set. The offset is localized around the Mg *b* lines. Figure 6 plots the velocity dispersion measured for the combined VIRUS-P wavelength regions used in the dynamical modeling (red circles) and the velocity dispersion calculated from just the Mg *b* region (green diamonds). Also plotted are the SAURON velocity dispersions for M87 (black squares). The SAURON spectral range is 4810–5310 Å and shows a similar offset to the VIRUS-P Mg *b* spectral region. To highlight this difference we have plotted, in Figure 5, the VIRUS-P spectra for five spectral regions, along with the template fits (red) and calculated velocity dispersion for each. For this particular spatial bin at $R = 24\farcs1$, the velocity dispersion determined from the Mg *b* region is lower than the mean of the other four regions by ∼30 km s^{-1}. This offset is not an outlier as can be seen in Figure 6. To place a number on this offset, we note that the average velocity dispersion of all the VIRUS-P data points between $7'' \leqslant R \leqslant 36''$ is 301.8 km s^{-1} when all four spectral regions used in the dynamical modeling are included as described in Section 3.1. The average velocity dispersion when using just the VIRUS-P Mg *b* region over the same spatial range drops to 281.8 km s^{-1}. Over the same spatial region ($7''$–$36''$) the average SAURON velocity dispersion is 287.0 km s^{-1}.

The cause for this offset is unknown and we do not attempt a detailed analysis of the offset here. Considering the good agreement between the SAURON and VIRUS-P results for the Mg *b* spectral range, and the different methods used by both data reduction pipelines to extract stellar kinematics, the offset is likely intrinsic to this spectral region. The issues surrounding the Mg *b* spectral region for determination of the velocity dispersion of elliptical galaxies, and the correlations with both galaxy luminosity and velocity dispersion are well known (Terlevich et al. 1981; Dressler et al. 1987; Worthey et al. 1992; Kuntschner et al. 2001). Barth et al. (2002) compare the velocity dispersion values measured from the Mg *b* and Ca triplet spectral regions for a sample of 33 local galaxies. They find that the Mg *b* region is more sensitive to changes in the fitting procedure than the

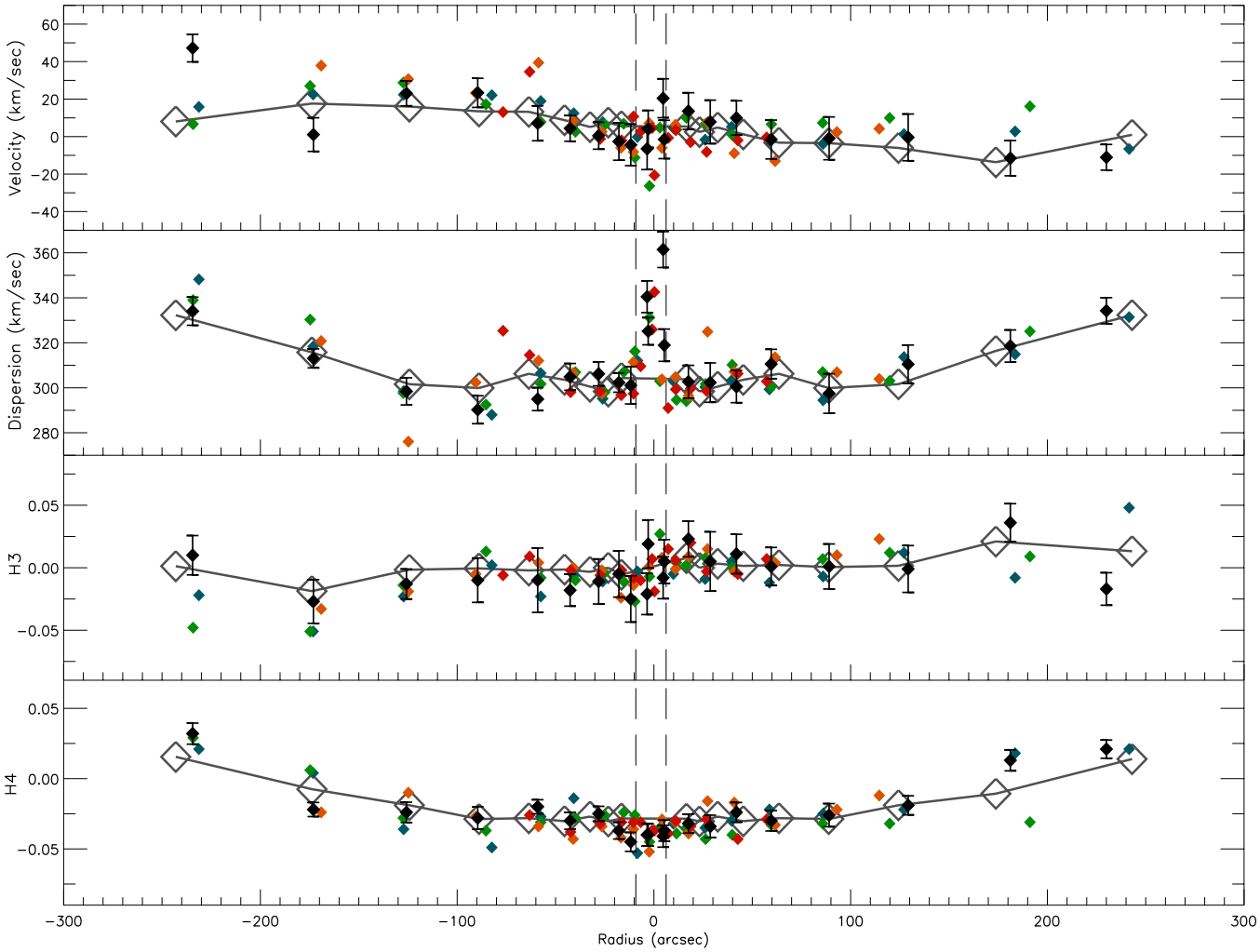

Figure 4. First four moments of the Gauss–Hermite expansion of the 88 VIRUS-P LOSVDs. The filled diamonds show the data at different angular bins. The black diamonds are for the major axis, followed by blue, green, orange, and with red along the minor axis. The dashed vertical lines near the center indicate the region where VIRUS-P data are not used and SAURON kinematics are employed in the modeling. The open diamonds, connected by a line, plot the moments, averaged over the angular bins, from the best-fit logarithmic dark halo model.

(A color version of this figure is available in the online journal.)

Ca triplet region, and exhibits an offset in velocity dispersion for 48% of the galaxies in their sample, yet with roughly equal numbers of galaxies showing higher velocity dispersion values from either one or the other spectral region. Barth et al. also compare the velocity dispersions of their Mg *b* region calculated when both including and excluding the 5150–5210 Å spectral window. For 32 of their 33 galaxies, they find lower velocity dispersion values when this region is suppressed from the fitting, with a clear trend toward a larger offset with higher galaxy velocity dispersion. We have explored this trend by suppressing a similar spectral region (5150–5220 Å) from our fitting and find similar results; velocity dispersion values calculated from the VIRUS-P spectra where the Mg *b* lines are withheld from the fitting are systematically lower than when these lines are included. However, the magnitude of our offset is small ($\sim$3 km s^{-1}) and is $\sim$10% of the offset seen by Barth et al. This discrepancy in the magnitude of the absolute offset value is likely due to differences in the two kinematic extraction routines used. Interestingly, it is in the *opposite* direction as naively expected from a comparison of the SAURON and VIRUS-P Mg *b* regions as excluding the Mg *b* lines leads to lower velocity dispersions, not higher ones. This suggests that the driving force behind the overall offset between the Mg *b* spectral region and the other four VIRUS-P spectral regions is not driven primarily by fits to the Mg *b* lines, but rather springs from issue in fitting that spectral region as a whole. A systematic study of various kinematic fitting methods over different spectral regions would be highly illuminating.

4. DYNAMICAL MODELS

We employ axisymmetric orbit-based dynamical modeling based on the idea first presented in Schwarzschild (1979). The specific details of our axisymmetric modeling can be found in Gebhardt et al. (2000, 2003), Thomas et al. (2004, 2005), and Siopis et al. (2009). The models have been shown accurate to $\sim$15% for recovery of the dark matter halo parameters (Thomas et al. 2005) and stellar M/L (Siopis et al. 2009). Several other groups have developed their own modeling based on Schwarzschild's orbit-based method. Dressler & Richstone (1988) and Rix et al. (1997) developed an orbit-based dynamical modeling code for spherical systems. van der Marel et al. (1998), Cretton et al. (1999), Gebhardt et al. (2000), and Verolme & de Zeeuw (2002) generalized to axisymmetric systems and van

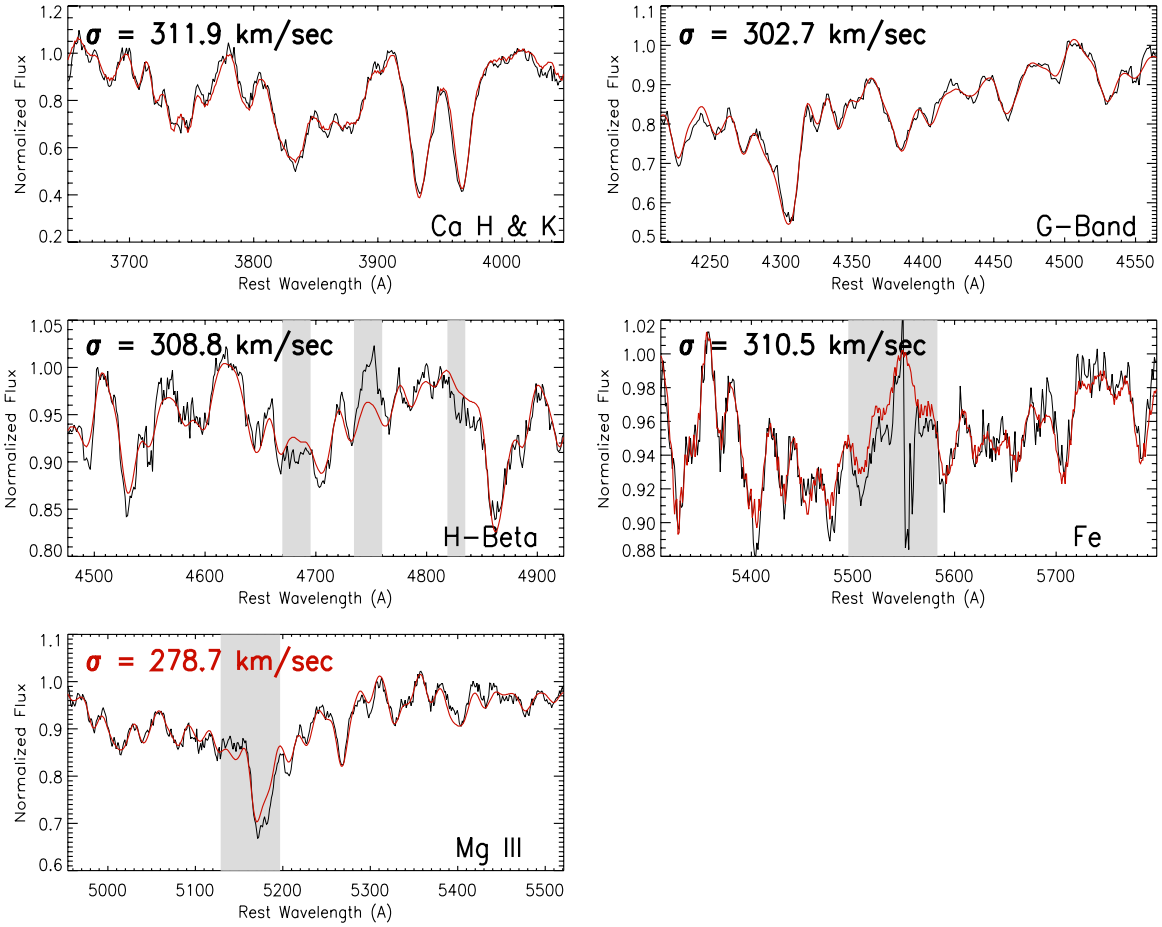

Figure 5. VIRUS-P data for five spectral regions from the spatial bin at $R = 24\farcs1$. The black line plots the data and the red line plots the best-fit stellar template. The shaded gray regions are withheld from the kinematic extraction as discussed in Section 3.1. The velocity dispersions measured for each of the five spectral regions are shown in the upper left of each panel. The systematic offset between the Mg b region ($\sigma = 278.7$ km s^{-1}) and the other four spectral regions (with a mean of $\sigma = 308.5$ km s^{-1}) is clear. The Ca H + K region, while initially withheld from the dynamical modeling due to a large systematic offset seen in its calculated Gauss–Hermite moments, is included here. The offset seen in Ca H + K was due to issues of continuum normalization. Since completion of the dynamical modeling this issue was resolved and can now be included in this comparison.

(A color version of this figure is available in the online journal.)

den Bosch et al. (2008) have developed a triaxial code. Now a number of groups have employed Schwarzschild's orbit-based method for black hole mass determination (Cretton et al. 1999; Verolme & de Zeeuw 2002; Cappellari et al. 2002; Gebhardt & Thomas 2009), stellar orbital structure and dark matter content (Cretton et al. 2000; Gebhardt et al. 2003; Copin et al. 2004; Krajnović et al. 2005; Cappellari et al. 2006; Thomas et al. 2007; Forestell & Gebhardt 2010).

We give an outline of the modeling procedure here. First, the galaxy's surface brightness is deprojected into a three-dimensional luminosity density. An edge-on inclination is assumed and so the deprojection is unique. Next, a trial gravitational potential is determined based on the three-dimensional light distribution and an initial guess for the stellar M/L, central black hole mass, and the dark matter halo parameters. Our orbit library is the same as used in GT09. The galaxy models extend to $2000''$ over 28 radial, 5 angular, and 15 velocity bins. The gravitational potential and force are calculated on a grid that is five times finer than the grid used to compare to the data. On average, 25,000 orbits are run in the trial gravitational potential. A superposition of these orbits is created that is both constrained by the light density profile and is a best match to the kinematic data. The superposition is accomplished by giving each orbit a weight as determined by maximizing the function $\hat{S} = S - \alpha\chi^2$. Here, S is an approximation to the Boltzmann entropy, χ^2 is the sum of squared residuals between the model and data LOSVDs (Equations (5) and (6)), and α is a smoothing parameter. See Siopis et al. (2009) for a detailed description of both the creation of the orbit library and determination of the orbit weights. The steps above are then repeated for a different model, each with a different stellar M/L, dark halo circular velocity, and scale radius.

Three types of models are run. First, we ran a set of dynamical models with no dark matter halo. As the only free parameter is the stellar M/L, only 100 models are needed to fully explore the parameter space. For the cored logarithmic halo (Equation (3)), we ran 6500 dynamical models. Over 8500 models are run assuming an NFW dark halo profile (Equation (4)). For each model, a distinct set of orbital weights is used and takes approximately 1.5 hours of cpu to run. We use the *Lonestar* computer at the Texas Advanced Computing Center (TACC) at The University of Texas, Austin to complete all our dynamical modeling.

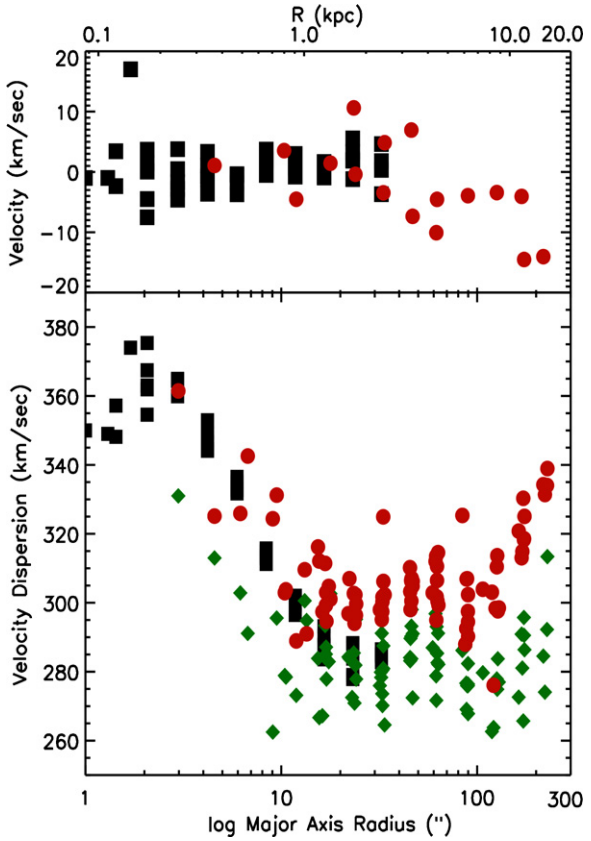

Figure 6. Velocity (top) and velocity dispersion (bottom) measurements from SAURON and VIRUS-P. Black squares plot the SAURON data and red circles the VIRUS-P data. The green diamonds show the velocity dispersion measured with VIRUS-P over the Mg *b* region. These velocity dispersion values are offset by ∼20 km s^{-1} from the velocity dispersion values calculated when combining spectral regions. With a wavelength range covering the H-beta and Mg *b* spectral regions, the SAURON spectral range is similar to the VIRUS-P Mg *b* region. The agreement between the SAURON and VIRUS-P velocity dispersion values over this region (277.0 km s^{-1} and 281.8 km s^{-1}, respectively) is within our uncertainties.

(A color version of this figure is available in the online journal.)

4.1. Model Assumptions

We calculate three types of dynamical models, each assuming a different mass distribution. First, we consider a mass model for M87 with no dark matter halo. The mass distribution (ρ) for these models takes the form

$$\rho(r) = \Upsilon\nu(r) + M_\bullet\delta(r), \tag{1}$$

where Υ is the stellar M/L, ν is the three-dimensional light density, and $M_\bullet$ is the black hole mass. As the black hole is better constrained from GT09 we set our black hole mass to $6.4 \times 10^9\,M_\odot$ for all our dynamical models. Gebhardt et al. (2011) have refined the black hole mass estimate of M87 to $6.6(\pm0.4) \times 10^9\,M_\odot$, yet this small change is within our uncertainties and does not change our results.

Both the second and third sets of dynamical models include a parameterization for a dark matter halo. The mass distribution then becomes a sum over each of the mass terms as follows:

$$\rho(r) = \Upsilon\nu(r) + M_\bullet\delta(r) + \rho_{\rm DM}(r), \tag{2}$$

where the first two terms are the same as in Equation (1), and $\rho_{\rm DM}(r)$ is the dark matter density term. Two different parameterizations for the dark matter halo are explored. The first is a logarithmic dark matter halo with a density profile as given by

$$\rho_{\rm DM}(r) \propto v_c^2\frac{3r_c^2 + r^2}{\left(r_c^2 + r^2\right)^2}. \tag{3}$$

The logarithmic halo features a flat central density core of size r_c and an asymptotically constant circular velocity, v_c. The physical motivation for the use of a cored logarithmic dark halo comes from observations of a wide range of galaxy types (see Donato et al. 2009 and references therein). The second dark matter density parameterization is an NFW profile (Navarro et al. 1996) as given by

$$\rho_{\rm DM}(r, r_s) \propto \frac{1}{(r/r_s)(1 + r/r_s)^2}. \tag{4}$$

The NFW halo diverges like r^{-1} toward the center and drops as r^{-3} with radius. The concentration (c), scale radius (r_s), and the virial radius (r_v) are related via $c = r_v/r_s$. Both dark matter parameterizations are included in the modeling as described in Thomas et al. (2005).

4.2. Modeling the Stars and Globular Clusters

The spatial grids used for the modeling are the same as in GT09. The spatial binning is split into $N_r = 28$ radial and $N_\theta = 5$ angular bins. Where the model bins are larger than the SAURON bins, we re-bin the SAURON data. The re-binning is accomplished by taking the average of all the LOSVDs falling within one model bin, weighted by their uncertainties. This complication does not arise with the VIRUS-P stellar data as we simply combine all the spectra from all fibers that fall within a given model bin *before* extraction of the LOSVD. For the central model bins ($R \lesssim 8''$), we elect to use just SAURON data for its superior spatial coverage. Between $8'' \leqslant R \leqslant 16''$ we use both SAURON and VIRUS-P data. We do not combine these data, but rather send in two LOSVDs independently into the dynamical modeling routines. A total of $N_{\mathcal{L}}^{\rm stars} = 25 + 80$ LOSVDs (SAURON + VIRUS-P) are used in the modeling, with each stellar LOSVD, $\mathcal{L}^{\rm stars}$, sampled by $N_{\rm vel} = 15$ velocity bins.

To determine the best-fit model, a χ^2 minimization is run in each trial potential. The χ^2 is calculated as

$$\chi^2_{\rm stars} = \sum_{i=1}^{N_{\mathcal{L}}^{\rm stars}}\sum_{j=1}^{N_{\rm vel}}\left(\frac{\mathcal{L}_{ij}^{\rm stars} - \mathcal{L}_{ij}^{\rm model}(\nu)}{\Delta\mathcal{L}_{ij}^{\rm stars}}\right)^2. \tag{5}$$

Here, $\mathcal{L}_{\rm ij}^{\rm model}(\nu)$ is the ith model LOSVD in the jth velocity bin. The orbit model is forced to reproduce ν, the stellar density, to machine precision. The residuals between the model and actual set of 105 LOSVDs are minimized for a single model potential, yielding a single $\chi^2_{\rm stars}$ value.

As the GCs can have a different orbital structure than the stars, they are treated as a separate kinematic component. The GCs are handled in a similar fashion as the stars, with the difference that we employ a deprojected number density for the GCs rather than the stellar luminosity density as for stars. Both the stars and GCs are then treated as massless test particles that orbit in a potential established by the assumed black hole mass, stellar M/L, and dark halo parameters. The weighted orbit superposition in each trial potential is determined by minimizing a similar equation as for the stars, namely,

$$\chi^2_{\rm GC} = \sum_{i=1}^{N_{\mathcal{L}}^{\rm GC}}\sum_{j=1}^{N_{\rm vel}}\left(\frac{\mathcal{L}_{ij}^{\rm GC} - \mathcal{L}_{ij}^{\rm model}(\nu)}{\Delta\mathcal{L}_{ij}^{\rm GC}}\right)^2, \tag{6}$$

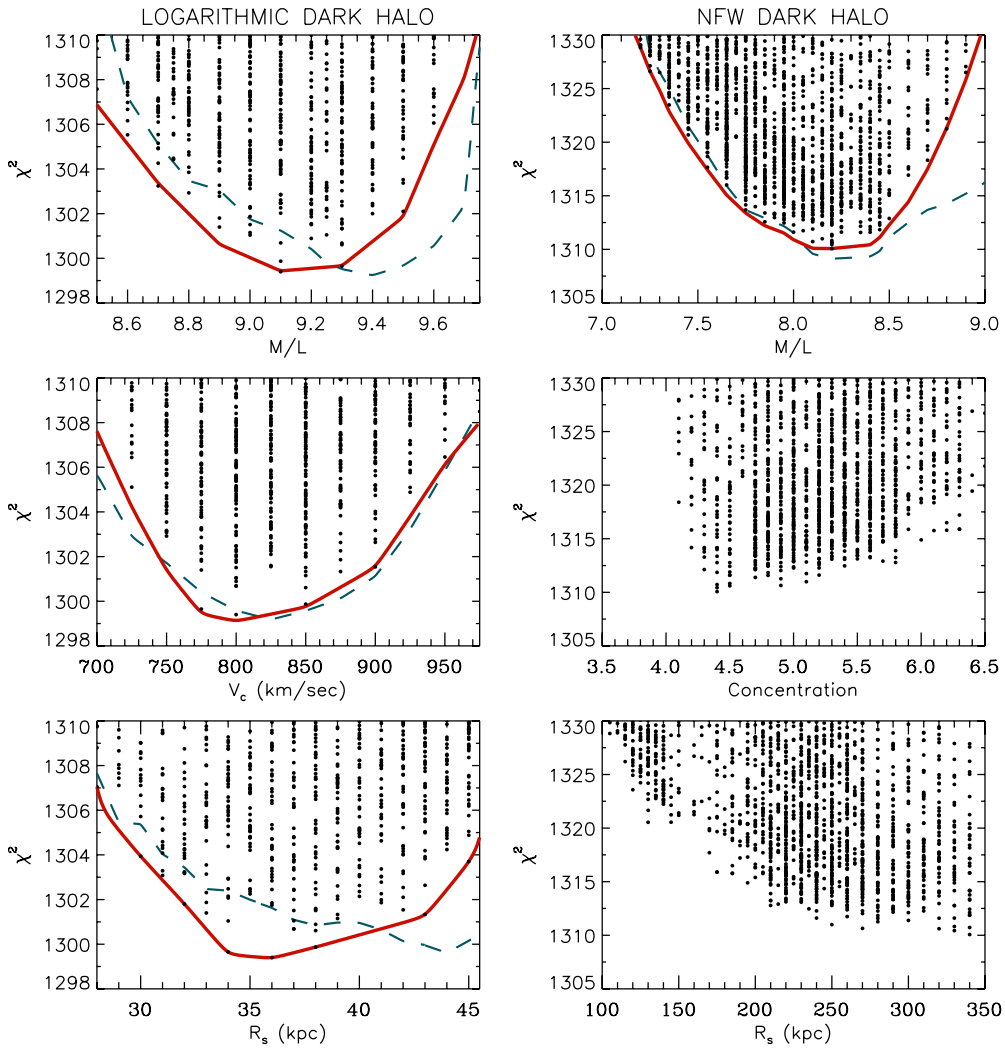

Figure 7. χ^2 values (stars + GCs) vs. the three modeling parameters for a logarithmic dark matter halo (left) and NFW halo (right). Each black dot is the χ^2 value from a single model. To highlight the variation at the χ^2 minimum, only a few hundred of the thousands of models run are shown. A smoothed spline fit to the minimum χ^2 values (plotted in red) gives us our 68% ($\Delta\chi^2 \leqslant 1$) and 95% ($\Delta\chi^2 \leqslant 2$) confidence bands. The dashed blue line plots the χ^2 minimum values for the stars. An additive shift of 41.5 has been made to the stellar values. As the shift is additive, the relative χ^2 values are preserved. The NFW halo results show the lack of constraint on the NFW scale radius parameter (lower right panel). We do not show similar spline fits to the NFW halo due to the unconstrained nature of the model. We note that while we do not constrain the NFW dark halo parameters, the constraint on the stellar M/L is very robust. The $\Delta M/L$ of 1.1 between the logarithmic and NFW models is due in large part to the difference in inner slope of the assumed dark halo parameters.

(A color version of this figure is available in the online journal.)

where $\mathcal{L}^{\rm GC}$ are the $N_{\mathcal{L}}^{\rm GC} = 11$ GC LOSVDs built up from individual GC velocities as described in Section 3.1. As with the stellar density, ν, the GC number density is reproduced to machine precision.

4.3. χ^2 Analysis

A χ^2 analysis is used to determine both the best-fit modeling parameters and their uncertainties. We can rule out a model with no dark matter with high confidence. The best-fit no dark matter model returns a stellar $M/L_{\rm v} = 11.4$. However, the χ^2 minimum for this model is 4898, which is a $\Delta\chi^2 \geqslant 3571$ increase over either of the best-fit models including dark matter. We do not discuss these models further. The best-fit models for both the logarithmic and NFW halos returns χ^2 minima of 1299.4 and 1310.1, respectively. The $\Delta\chi^2$ of 10.7 between the two dark matter parameterizations is statistically significant when comparing the different constraints we get on the stellar M/L. However, we do not get a constraint on either of the NFW dark halo parameters, concentration, and scale radius. This is clearly seen in the lower, right panel of Figure 7 where no clear χ^2 minimum for scale radius is seen out to 350 kpc. As our kinematic data do not extend beyond 50 kpc, we should not expect to get a constraint much beyond this radial distance. As we do not constrain the NFW dark halo, we focus here on the logarithmic halo results for our discussion of the χ^2 analysis, and refer to the NFW results where appropriate.

To select the best-fit dynamical model, we analyze the χ^2 values returned from each model run. The χ^2 values plotted in Figure 7 are the additive combination of the χ^2 values of both stars and GCs, namely, $\chi^2 = \chi^2_{\rm stars} + \chi^2_{\rm GC}$. Figure 7 plots these χ^2 values against the three model parameters for both the logarithmic and NFW dark halos. Each point gives the χ^2 value from a single dynamical model. The logarithmic dark halo parameters are plotted on the left. The solid red line is a cubic spline fit to the lowest χ^2 values along the parameter space. The dashed blue line shows the χ^2 minima coming from just the stars. For plotting purposes, an additive shift of 41.5 has been

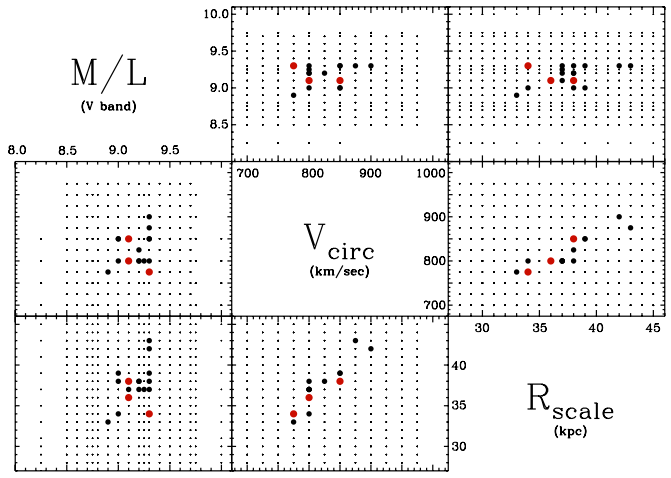

Figure 8. Plots of the χ^2 minimums of the three parameters plotted against one another for the logarithmic dark matter halo. The χ^2 range shown is the same as in Figure 7 (left half). The small black dots show individual models that lie near the χ^2 minimum. The larger black dots show models that fall within the 95% confidence band ($\Delta\chi^2 \leqslant 2$) while the larger red dots show models within the 68% confidence band ($\Delta\chi^2 \leqslant 1$). The modeling degeneracy between the dark and luminous matter, as discussed in GT09, is mitigated here due to the increased spatial coverage of VIRUS-P.

(A color version of this figure is available in the online journal.)

given to the dashed blue line. As the shift is additive, the relative χ^2 values are preserved.

On the right side in Figure 7, we plot the χ^2 values for the NFW models. We do not get a constraint on the NFW dark halo scale radius and concentration parameter. This is evident in the lower right panel of Figure 7 where the χ^2 minimum runs unconstrained to r_s values, well beyond the extent of our kinematic coverage. As the NFW concentration parameter is related to the scale radius as $c = r_v/r_s$, we also do not constrain this parameter.

In Figure 8 we plot the three modeling parameters against one another. These plots show the region centered on the χ^2 minimums for the logarithmic dark halo and help to explore degeneracies between the modeling parameterizations. The small black dots shown are the various models run located near the χ^2 minimum. The larger black dots plot models that fall within the 95% confidence band ($\Delta\chi^2 \leqslant 2$) and the red dots show models within our 68% confidence band ($\Delta\chi^2 \leqslant 1$). As the dynamical models constrain total enclosed mass, there exists the possibility of a degeneracy between the stellar M/L and the dark halo parameters. This degeneracy was clearly seen in Gebhardt & Thomas (2009) yet is substantially reduced in this work due to the improved spatial extent of the VIRUS-P data.

A total of 105 stellar LOSVDs and 11 GC LOSVDs are used in the dynamical modeling. Of the 105 stellar LOSVDs, 25 are determined from the four SAURON moments which provides $25 \times 4 = 100$ parameters. The 80 VIRUS-P LOSVDs used in the modeling are fit to 15 velocity bins, giving $80 \times 15 = 1200$ more parameters. The 11 GC LOSVDs are constructed from four parameters, giving another $11 \times 4 = 44$ parameters which totals to 1344 for each dynamical model. The best-fit dynamical model for a logarithmic halo had a $\chi^2 = 1299.4$, giving a reduced χ^2 value of 0.97. The χ^2 minimum for the NFW halo was 1310.1, which gives a similar reduced χ^2 value.

The constraints on stellar M/L come predominately from the stars, yet the GCs help to constrain the high M/L end as can be seen in the top left panel of Figure 7. This result is not surprising. The GC kinematics constrain the total enclosed mass in the outer modeling bins; their kinematics strongly influence the resulting dark matter halo mass. As we assume a constant M/L for the stars, mass not accounted for in the dark matter halo must get accounted for in the stars and drive the M/L to higher values. Therefore, kinematics that constrain the dark halo will also constrain regions of the modeling where that mass would otherwise wind up, namely, higher values for the stellar M/L.

In the lower left panel of Figure 7, we see a different influence of the GC kinematics stemming from their extended spatial coverage. Constraints on higher r_s values come from the GC kinematics, which extend to 47 kpc. This result is expected, as the stellar kinematics do not extend out to the dark halo scale radius and can therefore not influence the modeling. Clearly, the GC kinematics are important for constraining the dark halo parameters, and the good agreement between the best-fit stars + GC model and the stars-only model, where the kinematics overlap, is reassuring since it implies that both large radii stars and GCs are in dynamical equilibrium. Further evidence for equilibrium between the large radii stars and GCs is seen in the excellent agreement in their velocity anisotropy (see Section 5.3 and Figure 12).

The $\Delta\chi^2 = 1$ range gives us the 68% confidence bands for each of the three parameters. For the logarithmic dark halo, the best-fit stellar M/L is $9.1^{+0.2}_{-0.2}$ (V band). The best-fit dark matter halo circular velocity is 800^{+75}_{-25} km s^{-1}, and dark matter halo scale radius is radius of 36^{+7}_{-3} kpc. The NFW dark halo, while not constrained, still gives a robust estimate of the stellar M/L of $8.20^{+0.05}_{-0.10}$. The difference in these stellar M/L values is driven entirely by the shape of the assumed dark halo, and that the dynamical models work by constraining total enclosed mass. As the NFW halo allows for a higher central concentration of mass, and the stellar M/L is assumed constant as a function of radius, mass can be taken up by the cuspier NFW profile, thus lowering the M/L of these models.

5. DISCUSSION

The parameters of the dark halo from this paper are different than the ones presented in GT09 which is also based on a stellar dynamical analysis. GT09 also fit a cored logarithmic dark matter halo yet find a circular velocity that is 10% lower and a scale radius that is 60% lower than these results. The reason for the difference is due to the data sets; the data presented here have substantially improved kinematic coverage for the stars. The stellar kinematics of GT09 end at 33″ whereas our coverage extends to nearly 240″. The GC data are identical between the two papers. The large gap in kinematic spatial coverage in GT09 between 33″ and 140″ leads to generally poor constraints on the dark matter halo parameters. The new VIRUS-P data close this gap and are therefore more robust.

5.1. Enclosed Mass

The best-fit dark matter halo parameters for a cored logarithmic profile return 800^{+75}_{-25} km s^{-1} for circular velocity, and 36^{+7}_{-3} kpc for the scale radius. In terms of enclosed mass, M87's dark matter halo is one of the largest ever measured for an individual galaxy. Figure 9 plots enclosed mass for our best-fit logarithmic and NFW models. The black and red lines, with uncertainty, plot total enclosed mass for the logarithmic and NFW models, respectively. The inclusion of a $6.4 \times 10^9\ M_\odot$ black hole keeps the total enclosed mass from reaching zero at

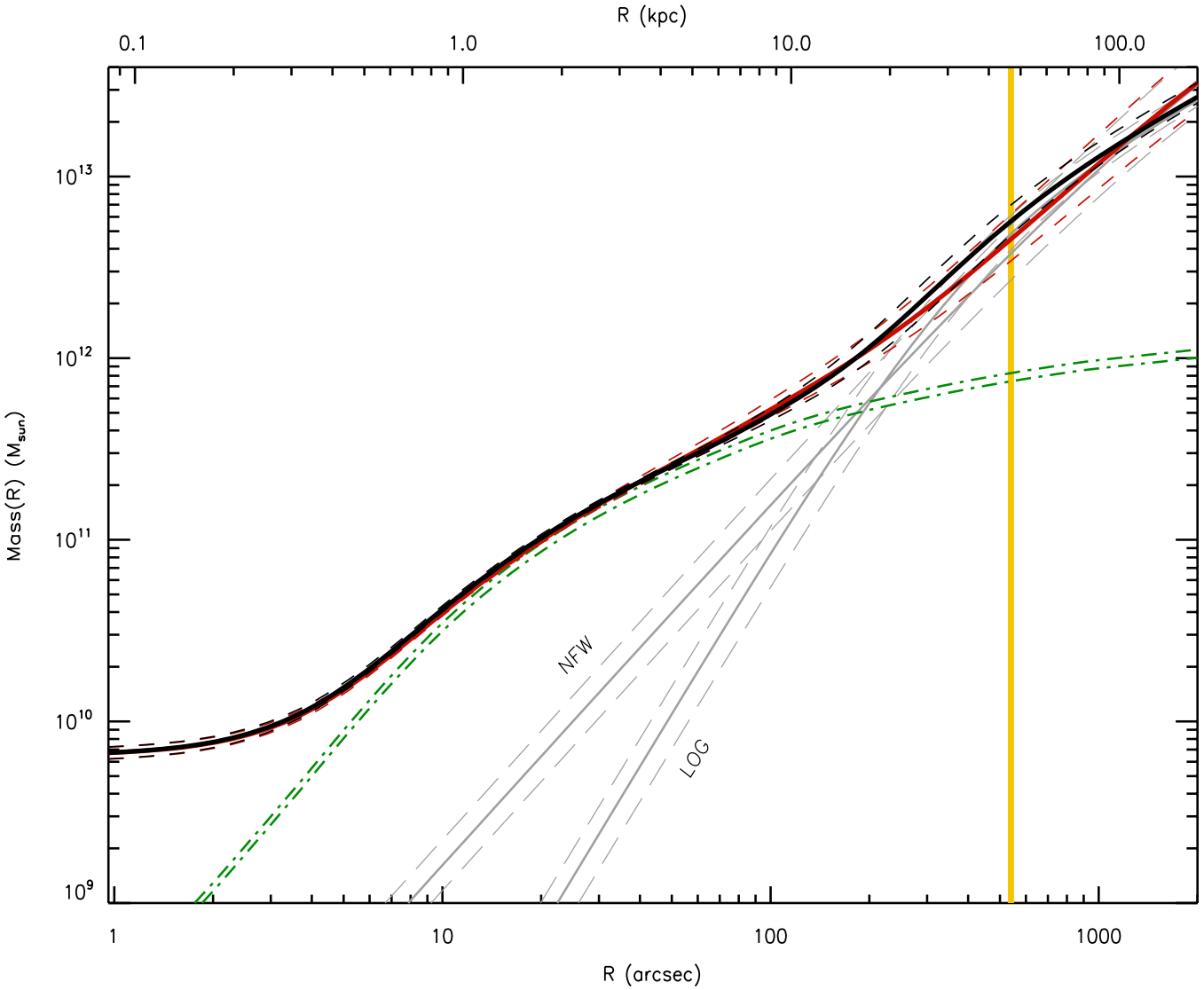

Figure 9. Total enclosed mass as a function of radius. The solid, black line indicates total enclosed mass for our best-fit logarithmic model. The NFW enclosed mass profile is plotted in red. Both of these enclosed mass models are plotted with uncertainties, which are the min/max values for the $4^2 = 16$ dynamical models that explore the parameter limits of our 68% confidence bands. The green lines plot stellar mass for both models (with uncertainties less than the thickness of the line) and the light gray lines, with uncertainties, indicate the two assumed dark matter distributions. Note the total enclosed mass does not go to zero with radius due to inclusion of a $6.4 \times 10^9\ M_\odot$ mass black hole. Modeling results beyond our last data point, indicated by the vertical yellow line, are not constrained by the data, and are therefore suspect.

(A color version of this figure is available in the online journal.)

$R = 0$. The uncertainties are the min/max values for the $4^2 = 16$ dynamical models that explore the parameter limits of our 68% confidence bands. For the uncertainty in the black hole mass we use the $\pm 0.5 \times 10^9\ M_\odot$ values from GT09. The stellar component is plotted in green (dot dash) with uncertainties within the thickness of the lines. The dark matter profiles are plotted in gray (long dash). The yellow vertical line shows the extent of our kinematic data. The comparison between the enclosed mass model from the best-fit logarithmic and NFW halos shows good agreement to the end of our stellar kinematics. The NFW enclosed mass profile then begins to diverge to lower total enclosed mass to the end of our kinematic coverage. We discuss how our results compare to other mass estimates for M87 in Section 5.2.

The degree to which the GCs help to constrain the dark matter profile can be seen in another light in Figure 10 where we plot the enclosed dark matter fraction for the logarithmic dark matter halo. The solid red line shows the dark matter fraction when including both GC and stellar kinematics in the analysis. The dashed blue line comes from an analysis of the stars only. It is clear that kinematics at large radii are essential to a robust determination of the dark matter fraction at all radii beyond the central 0.3 R_e.

5.2. Comparison to Other Mass Estimates

At larger radii Doherty et al. (2009) have measured kinematics of PNe for M87. They find a dark halo consistent with the one presented here inside of 500″, although since their radial range is 400″–2500″ there is not much spatial overlap with our current data set. At around 600″ they find that the mass density begins to decrease strongly, leading to a truncation of M87's dark halo. At $R = 1500''$, their outermost radial bin, the PNe dispersion they measure is 78 ± 25 km s^{-1}. For the spatial overlap between our work and theirs (400″–540″), where we are now comparing

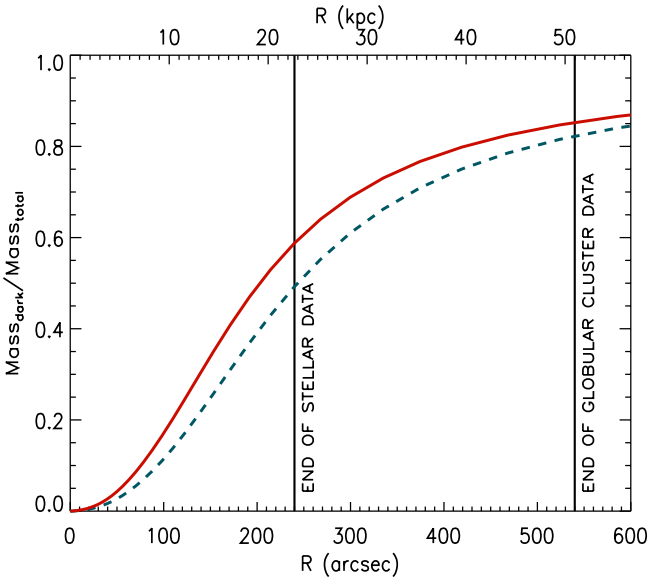

Figure 10. Enclosed dark matter fraction as a function of radius for a logarithmic halo. The red (solid) line shows the best-fit χ^2 model for both stars and globular clusters (i.e., $\chi^2 = \chi^2_{\rm stars} + \chi^2_{\rm GC}$). The blue (dashed) line shows the best-fit dynamical model based on the χ^2 value for stars only (i.e., $\chi^2 = \chi^2_{\rm stars}$). This figure indicates the degree to which the large radii GCs influence the dark matter fraction at all radii.

(A color version of this figure is available in the online journal.)

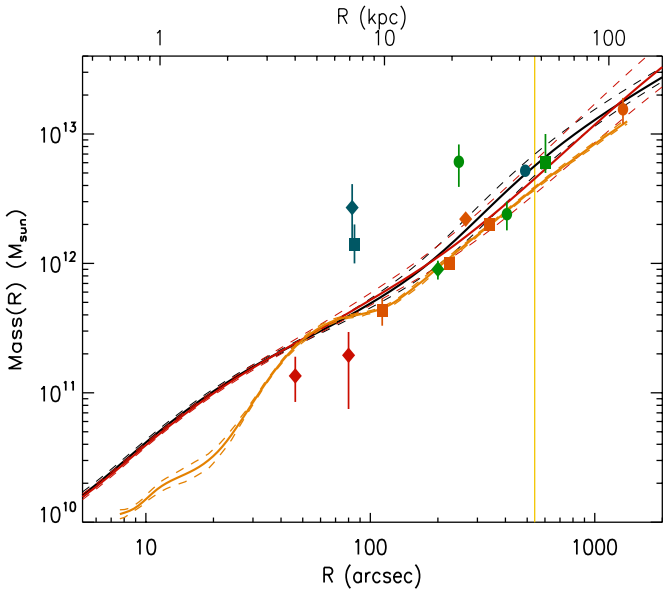

Figure 11. Comparison of total enclosed mass from the literature. The symbols are explained in Table 4. The color of the symbols indicates the method employed to make the mass determination. Blue: empirical, green: GC kinematics, red: stellar kinematics, orange: X-rays. The red, black, and yellow lines are described in Figure 9.

(A color version of this figure is available in the online journal.)

GCs and PNe, the kinematics disagree. Possible reasons for the disagreement are that the GC kinematics in this region are poorly measured or that the GCs are not in dynamical equilibrium (e.g., from a recent merger event). Both Cohen (2000) and Côté et al. (2001) find that the GC population around M87 shows both chemical and kinematic evidence for two distinct populations of GCs. Another possibility is that the PNe measurements are biased in some way. Doherty et al. (2009) exclude three of eight PNe for their $R = 800''$ bin as intracluster PN and not tracing the potential of M87. Including these three PNe raises their measured dispersion from 139 km s^{-1} to 247 km s^{-1}. Certainly a comparison to either GC or stellar kinematics at this radial position would be enlightening.

Wu & Tremaine (2006) estimate the enclosed mass of M87 at 32 kpc (35.1 kpc at our assumed distance) to be $2.4(\pm0.6) \times 10^{12}\ M_\odot$ using GC kinematics and assuming spherical symmetry. Our mass estimate of $3.64^{+0.87}_{-0.65} \times 10^{12}\ M_\odot$ (logarithmic halo) at this radial position falls within the uncertainties, yet with an offset of ∼34%. Romanowsky & Kochanek (2001), using stellar kinematics from van der Marel (1994) and Sembach & Tonry (1996), and GC kinematics from several sources, derive an enclosed mass profile for M87 that shows a similar offset toward lower total mass over the range $1\ R_e \leqslant R \leqslant 5\ R_e$. Within $1\ R_e$ their models diverge to ∼50% lower total mass. This discrepancy may be due to the stellar kinematics used over this radial range. The stellar kinematics of Sembach & Tonry exhibit a systematic offset from other data sets for which Romanowsky & Kochanek make a correction. The offset between our enclosed mass and theirs within $1\ R_e$ may be due to this effect or due to the different modeling assumptions, as Romanowsky et al. assume spherical symmetry for their modeling. The discrepancy may also come about due to the increase in spatial coverage the VIRUS-P data afford over their long-slit spectroscopy.

Comparison of the X-ray mass determination from Das et al. (2010) to our mass profile from stars and GCs shows good agreement over the range $4\ \text{kpc} \leqslant R \leqslant 20$ kpc, yet diverges elsewhere (see Figure 11). At both larger and smaller radii, the mass profile from X-rays is lower than that determined by the stars and GCs. At $R = 3$ kpc, the X-ray estimated mass is down by 50% and at $R = 2$ kpc the disagreement is ∼70%. A similar discrepancy is seen at larger radii. The enclosed mass from X-rays at $R = 47$ kpc, our furthest data point, is lower by 50% than our best-fit value. This difference is similar to the one seen in NGC4649 (Shen & Gebhardt 2010). One possible explanation for this discrepancy comes from allowing for a turbulent component in the X-ray gas. A 50% decrease in enclosed mass can be explained by a ∼30% non-gravitational component in the gas. This amount of difference is similar to the theoretical expectation of Brighenti & Mathews (2001) and has been seen in similar systems (Churazov et al. 2010). More analysis on a wider set of galaxies is necessary to fully understand the source of these differences.

In Table 4 and Figure 11, we compare enclosed mass estimates from the literature to this work. Our logarithmic and NFW halo mass profiles are plotted as in Figure 9. Each colored symbol in Figure 11 indicates the methods employed to determine the enclosed mass. In general, we find a more massive dark halo for both our logarithmic and NFW parameterizations, although our enclosed mass values at various radial positions are not consistently the highest reported in the literature and appear consistent with the scatter of the data seen in Figure 11.

5.3. Stellar Anisotropy

The mechanisms by which mass accumulation occurs in galaxies leave their mark on the distribution function of the stars (Lynden-Bell 1967; Valluri et al. 2007). Therefore, mapping the anisotropy of both the stars and GCs can address questions surrounding galaxy formation history and evolution. Our orbit-based dynamical modeling returns the stellar orbital structure, which we summarize in Figure 12. Plotted is the average velocity anisotropy over the 20 angular modeling bins of

Table 4
Literature Mass Comparison

Reference (year)	Method	Symbol	Radius (arcsec)	Literature ($10^{12}\ M_\odot$)	Logarithmic ($10^{12}\ M_\odot$)	NFW ($10^{12}\ M_\odot$)
Nieto & Monnet (1984)	Empirical	Circle	490	5.20	$4.90^{+1.14}_{-0.82}$	$3.90^{+1.39}_{-0.91}$
Brandt & Roosen (1969)	Empirical	Diamond	84	$2.7^{+1.4}_{-1.4}$	$4.07^{+0.28}_{-0.25}$	$4.30^{+0.49}_{-0.34}$
Poveda (1961)	Empirical	Square	84	$1.4^{+3.4}_{-0.4}$	$0.42^{+0.03}_{-0.03}$	$0.44^{+0.05}_{-0.03}$
Fabricant & Gorenstein (1983)	X-rays	Circle	1336	$15.5^{+3.5}_{-3.5}$	$17.9^{+3.3}_{-1.6}$	$18.3^{+8.9}_{-5.2}$
Huchra & Brodie (1987)	GC kinematics	Circle	248	$6.1^{+2.2}_{-2.2}$	$1.61^{+0.35}_{-0.29}$	$1.47^{+0.37}_{-0.26}$
Mould et al. (1987)	GC kinematics	Diamond	200	$0.90^{+0.15}_{-0.15}$	$1.15^{+0.22}_{-0.18}$	$1.12^{+0.25}_{-0.17}$
Sargent et al. (1978)	Stellar kinematics	Diamond	80	$0.19^{+0.10}_{-0.20}$	$0.39^{+0.03}_{-0.02}$	$0.41^{+0.05}_{-0.03}$
Sargent et al. (1978)	Stellar kinematics	Diamond	47	$0.14^{+0.05}_{-0.05}$	$0.24^{+0.01}_{-0.01}$	$0.24^{+0.02}_{-0.01}$
Tsai (1996)	X-rays	Diamond	266	2.20	$1.80^{+0.41}_{-0.33}$	$1.61^{+0.42}_{-0.29}$
Merritt & Tremblay (1993)	GC kinematics	Square	603	$6.0^{+4.0}_{-1.0}$	$6.66^{+1.50}_{-0.99}$	$5.36^{+2.07}_{-1.32}$
Matsushita et al. (2002)	X-rays	Square	113	$0.43^{+1.0}_{-1.0}$	$5.58^{+0.58}_{-0.50}$	$5.92^{+0.85}_{-0.60}$
Matsushita et al. (2002)	X-rays	Square	226	$1.0^{+1.0}_{-1.0}$	$1.39^{+0.29}_{-0.24}$	$1.30^{+0.32}_{-0.21}$
Matsushita et al. (2002)	X-rays	Square	340	$2.0^{+1.0}_{-1.9}$	$2.71^{+0.65}_{-0.50}$	$2.26^{+0.69}_{-0.46}$
Wu & Tremaine (2006)	GC kinematics	Circle	406	$2.4^{+0.6}_{-0.6}$	$3.64^{+0.87}_{-0.65}$	$2.93^{+0.97}_{-0.65}$

Notes. Enclosed mass values from the literature. Column 1: Reference. Column 2: Method employed to determine enclosed mass. Column 3: Symbol used to plot the data in Figure 11. Column 4: Radial distance from the center of the galaxy, scaled to the distance assumed in this work ($R = 17.9$ Mpc). Column 5: Literature value of enclosed mass at the radial position in Column 4. The uncertainty is quoted, where available. Column 6: Enclosed mass from the best-fit logarithmic halo model from this work. Column 7: Enclosed mass from the best-fit NFW halo model from this work.

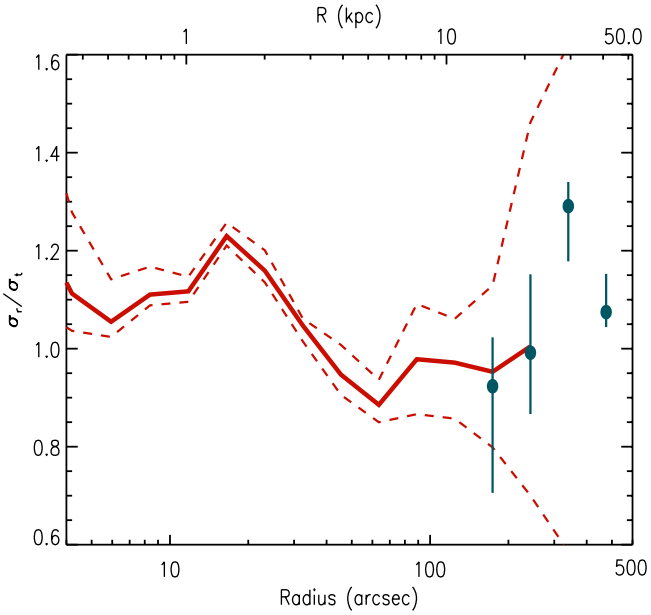

Figure 12. Ratio of the radial velocity anisotropy to the tangential anisotropy for both the stars (red lines) and GC (blue dots).
(A color version of this figure is available in the online journal.)

both the stars and GCs. The uncertainties are calculated in the same way as described in Figure 9 and the text. Within $R \simeq 0.5\ R_e$ the stars show radial anisotropy, then become mildly tangentially anisotropic to the last stellar data point. The excellent agreement between the stars and GCs in this region is indicative of dynamical equilibrium between these two components. Although we do not conduct a detailed analysis of the anisotropy of M87 here, comparison of anisotropy maps to *N*-body simulations can be highly informative. An example of such an analysis can be found in Hoffman et al. (2010) where the dynamical modeling of NGC4365 by van den Bosch et al. (2008) is compared *N*-body simulations.

5.4. A Discussion of Systematic Uncertainties

Given the high S/N of our data, we pay particular attention to quantifying systematic uncertainties, since they might be important for the reported uncertainties. As we are using $\Delta\chi^2$ to determine the parameter values and uncertainties, if we do not have proper uncertainty estimates for the kinematics we will bias our final modeling results. There are three internal consistency checks that demonstrate that our uncertainties are properly estimated.

First, we estimate LOSVDs and Gauss–Hermite parameters from four different wavelength regions. Comparing the standard deviation across the four regions to the individual uncertainties from the Monte Carlo simulations provides a consistency check. We find that, in general, these two uncertainties estimates are consistent. The large wavelength range of VIRUS-P provides this very important estimate, which includes both statistical and systematic effects.

Second, the reduced χ^2 for the best-fit dynamical models is near unity. The χ^2 is measured from the LOSVDs, and we can see the agreement in the plot of observed and modeled moments (Figure 4). The deviations between the data and the modeling moments are consistent with the stated uncertainties. While this consistency does not directly show that systematic effects are not an issue, it is an indirect confirmation.

Third, when comparing kinematics from data sets taken at different times we find consistent results within the stated uncertainties. With the spatial overlap of our pointings 3 and 4 we are able to compare the resulting kinematics from four of our spatial bins when taken a year apart. We have compared the first four Gauss–Hermite moments, calculated from our extracted LOSVD, and find that they are all consistent within their stated uncertainties. These three internal checks demonstrate control of the measured uncertainties.

Next, we discuss the two areas where systematic effects may be important: sky subtraction and template mismatch. In order to determine how the level of sky subtraction affects our extracted kinematics and subsequent modeling, we explore both

over and under subtraction of each 20 minute science frame. A range of sky subtraction levels are created and taken through all subsequent data reductions. A total of 25 different sky subtractions are made on each science frame, over a range of $\pm 12.5\%$ when compared to equal exposure times. The details of these reductions are given in the *Sky Subtraction* section in the Appendix. We then compare the calculated velocity and velocity dispersion values, taken from the best-fit LOSVD. This comparison, over all 88 spectra, shows no systematic offsets in velocity or velocity dispersion for either over or under subtraction of the night sky. The associated random errors for this full range of sky subtractions is within our quoted uncertainty for both velocity and velocity dispersion.

In order to explore possible systematics due to our use of the Indo-US spectral library, we select the same set of template stars from the Miles spectral library (Sánchez-Blázquez et al. 2006) and extract kinematics for all of our spectra. The two libraries agree very well, with deviations between the libraries of $\sim 2.5\ \mathrm{km\ s^{-1}}$, well within our quoted uncertainties for velocity dispersion. In the case of velocity, there is a slight offset ($\sim 7\ \mathrm{km\ s^{-1}}$) which is due to the lack of a velocity zero point between the two libraries. Both of these checks indicate that our systematics are under control.

5.5. Next Steps

This work points the way to several other areas of inquiry. We have explored two different parameterizations for a dark matter halo, yet others exist and there is no reason to dismiss any of them. A natural next step is to rigorously explore several different dark matter halo parameterizations with the same data sets and modeling methods to determine which, if any, is favored. This requires us to push the collection of stellar kinematics to ever larger radii. The amount of observation time needed to reach to 2.4 R_e with VIRUS-P was not substantial, and stellar kinematics to 3 and 4 R_e are achievable. These data would allow for both better constraints on the various dark matter halo parameters and a comparison with the other dynamical tracers (i.e., GCs and PNe). As much of our current understanding of the dark matter halos around elliptical galaxies depends on GC and PNe kinematics, a robust comparison between each tracer is needed to explore systematics.

A second avenue of exploration comes from the information contained in the stellar chemical abundances available through a Lick index analysis. Graves & Schiavon (2008) provide a publicly available tool that is well suited for this work. How elliptical galaxies formed and whether their stars were formed in situ or accreted over time requires both a dynamical and chemical analysis (Graves & Faber 2010). The chemical composition of GCs at large radii has been studied (Cohen 2000; Côté et al. 2001), and a detailed comparison of both the kinematics and chemistry of both GCs and stars at the same radial position should prove immensely fruitful.

Finally, work toward a more complete and uniform sample of massive elliptical galaxies, both first- and second-rank galaxies, and equally massive field ellipticals (e.g., NGC1600) is needed to explore the influence of environment on dark matter halos. Several groups have made significant progress toward this end, yet the data sets that involve both two-dimensional spatial coverage at both small and large need to be expanded.

The authors thank The Cynthia and George Mitchell Foundation for their generous support which made the fabrication of VIRUS-P possible. J.D.M. thanks the members of his research committee: Michele Cappellari, Gary J. Hill, John Kormendy, Phillip J. MacQueen, and Miloš Milosavljević for all the help given. J.D.M. also thanks Guillermo Blanc, Ross E. Falcon, and Remco van den Bosch for their insight and many fruitful discussions. The authors also thank Dave Doss, Kevin Meyer, Brian Roman, John Kuehne, and all of the staff at the McDonald Observatory who helped immensely with the commissioning of VIRUS-P and the successful collection of this data. This research is partially based on data from the publicly available SAURON Archive, which aided substantially in the modeling. The authors thank Payel Das and her collaborators for their willingness to share their X-ray data and analysis on M87. This work would not have been possible without the resources of the Texas Advanced Computing Center at the University of Texas, Austin where all of the dynamical modeling was run.

APPENDIX

DATA REDUCTION

The reduction of integral field spectroscopy (IFS) data involves numerous issues not faced in the reduction of traditional long-slit data (Barden & Wade 1988; Parry & Carrasco 1990; Wyse & Gilmore 1992; Barden et al. 1993; Lissandrini et al. 1994; Watson et al. 1998). Each fiber exhibits its own character, with variations in spatial PSF, transmission, and focal ratio degradation (Avila 1988; Ramsey 1988; Bershady et al. 2004; Murphy et al. 2008). Despite these complications, many groups have developed robust and versatile pipelines for the reduction of IFS data(Bacon et al. 2001; Zanichelli et al. 2005; Turner et al. 2006; Sánchez 2006; Sandin et al. 2010).

This paper is the first in a series and establishes our principle methods of data reduction. For this reason, we give a detailed description of each step in the data reduction process. In the description below, the term "spectral" is used to indicate the wavelength or the *X*-direction on the CCD. The term "spatial" is used for the cross-dispersion or the *Y*-direction.

A.1. Reduction Details

The preliminary data reduction uses Vaccine (Adams et al. 2011), an in-house pipeline developed for reduction of VIRUS-P data. We give a full account of the Vaccine data reduction steps here. First, the overscan and bias are subtracted from all frames. The CCD is very clean, therefore no masking of bad pixels is conducted. Next, the twilight flats and arc lamp frames are combined with the biweight estimator (Beers et al. 1990). The biweight is used at several steps in the reduction process.

Due to issues of instrumental alignment and the inherent limitations of all optical elements, curvature in both the spatial and spectral directions on the CCD is unavoidable. The curvature along the spatial direction is handled by allowing each fiber to have its own wavelength solution. In order to correct for the curvature along the spectral direction, the twilight flats are used to locate the centers of each fiber and determine the fiber *trace*. To accomplish this, a 21 pixel-wide boxcar is run along a single fiber of the twilight flat in the spectral direction. The fiber profile in the spatial direction is super-sampled with the boxcar and fit with a Gaussian profile to determine the center of the fiber at each pixel step in the spectral direction. This boxcar method effectively smooths over fiber spatial profile variation due to solar absorption features and pixel-to-pixel flat-field variation while giving a robust estimate of the location of the center of the Gaussian profile. As the curvature in the spectral direction is not extreme ($\sim \Delta 5$ pixels from the center of the CCD to the edge

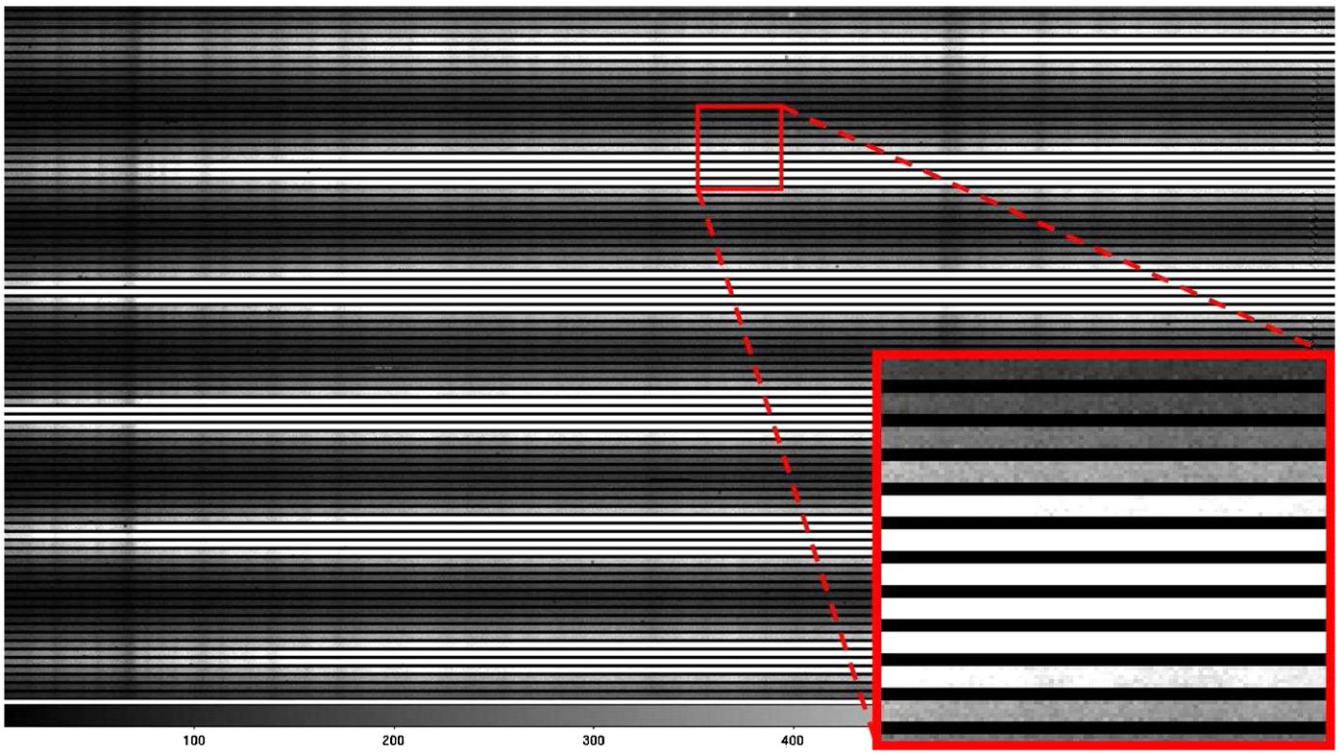

Figure 13. Image of VIRUS-P data from a 20 minute central pointing on M87 (no. 3 in Figure 1) after all preliminary data reduction is complete. Just the central ∼90 fibers are shown. The inset shows a close-up of 11 fibers extracted over a 5 pixel-wide aperture. Residuals from the 5577 Å sky line subtraction can be seen to the far right. The strong absorption feature seen on the far left is the *G* band (∼4310 Å rest frame). The weaker absorption band near the center, just to the left of the small box, is H_β (∼4860 Å) and the strong, wide feature toward the right is the Mg *b* region (∼5167–5183 Å).

(A color version of this figure is available in the online journal.)

of the 2048 × 2048 chip) a 21 pixel-wide boxcar smoothing is justified. The location of the centers of all the Gaussian profiles for a single fiber are then fit with a fourth-order polynomial. The polynomial fit becomes the *trace* of the fiber. The steps described above are repeated for all 246 fibers.

Once the fiber trace is determined for all 246 fibers, the fiber profile is extracted, fiber by fiber, over a 5 pixel-wide aperture. Figure 13 shows an image of the central ∼90 fibers of a typical frame after extraction. As the fiber centroid moves from one row of pixels to the next the 5 pixel extraction aperture follows. By allowing the extraction aperture to make discrete steps between rows of pixels we avoid interpolation of the data. There are two advantages to not resampling the data at this step. First, we avoid introducing the correlated noise inherent to interpolation and can therefore carry accurate pixel-to-pixel noise calculations through the final step of the Vaccine reductions. This is helpful as a proper S/N calculation is necessary for the Monte Carlo error estimations made later in the reductions (Section 3.2). Second, interpolation can artificially broaden the spectra, and while the dispersion of M87 is well above the instrumental dispersion for all our pointings, this should not be assumed a priori.

The typical FWHM of a fiber profile along the spatial direction is ∼4 pixels with an average spacing of ∼8 pixels between the centers of adjacent fibers. We have measured the cross-talk between fibers to be $\leqslant$1% over a 5 pixel-wide aperture. The fiber position on-sky is mapped onto the CCD from left to right and top to bottom (Figure 2). Therefore, neighboring fibers on the CCD are typically neighboring fibers on the sky and, as neighboring fibers are often combined to reach the desired S/N, the effect of cross-talk is further mitigated. We explored extracting over a 7 pixel-wide aperture and compared the final S/N of both extractions. Due to the low level of signal in the edges of the 7 pixel aperture, the 5 pixel aperture returns better S/N and is used for all VIRUS-P data presented here.

Mercury and cadmium arc lamp frames are used for wavelength calibration and afford eight unblended and well-spaced emission lines over our wavelength range. The wavelength of each emission line has been confirmed using the Robert G. Tull Coudé spectrograph on the 2.7 m telescope in the $R = 60$ k setup. The wavelength solution for each fiber is determined as follows. For an individual fiber, each emission line is fit with a Gaussian profile to determine its center.[2] A fourth-order polynomial is fit to the centers of each emission line and the residuals between the actual wavelength and fit wavelength are minimized. The cadmium 3611.3 Å line and the mercury 5769.6 Å line are near the blue and red edges of our wavelength range and minimize the amount of extrapolation needed at the edges of the polynomial fit. Typical rms residuals of the polynomial fit are $\leqslant$0.07 Å or $\leqslant$4.4 km s^{-1} at 4800 Å (FWHM). Comparison of the wavelength solution from the arc lamps taken at the start and end of the night show differences well below the noise of the fit. We find that small linear shifts in the spectral direction of the fiber, possibly due to thermal variations at the output end of the fibers, can occur on the timescales of an hour. To account for this shift, a correction is made to the zeroth-order term of the wavelength solution based on the change in position of the bright 5577.34 Å sky line. The average of this correction over

[2] We have characterized the spectral PSF of the VIRUS-P instrument and find it to be very nearly Gaussian. To quantify this, we fit Gauss–Hermite coefficients to four bright lines in our mercury–cadmium arc lamp frames. Over the four spectral lines and all 246 fibers the median H3 coefficient is 0.003 ± 0.013, while the median H4 coefficient is 0.0003 ± 0.0117.

all frames was 0.13 Å with a standard deviation of 0.11 Å. A heliocentric correction is made to each frame. For our February data, this correction had a mean of 19.3 km s^{-1} and a standard deviation of 0.7 km s^{-1}. For our January data, the mean heliocentric correction is 27.6 km s^{-1} with a standard deviation of 0.2 km s^{-1}.

The next reduction step involves creating a flat-field frame from the twilight flats. There are four different pieces of information combined in the twilight flats: pixel-to-pixel variation, fiber-to-fiber throughput variation, fiber cross-dispersion profile shape, and the twilight sky spectrum. The first three are aspects of the flat field we want to preserve while the twilight sky spectrum must be removed. Our approach is to construct a model of the twilight sky, free of flat-field effects, and then divide this model out of the original twilight frame. To generate a model of the night sky, we use a method similar to Kelson (2003) for IFS sky subtraction. We outline our method here.

To model the twilight sky a 51 fiber-wide boxcar is run along the spatial direction. As each fiber has a slightly different wavelength solution, a B-spline interpolation (Dierckx 1993) of the pixel's wavelength is made, based on the wavelength solution determined by the arc lamp polynomial fits. By employing a B-spline interpolation, we are not limited by the pixelization of the wavelength solution. The 51 fiber-wide boxcar and 5 pixel-wide extraction aperture provides $51 \times 5 = 255$ estimates of the twilight flux at a given wavelength. Both pixel-to-pixel, fiber throughput, and fiber profile shape vary on scales much smaller than the size of the boxcar and are thus smoothed out. What remains is a model of the twilight sky with flat-fielding effects removed. The model is then divided out of the original twilight flat, leaving pixel-to-pixel, fiber throughput, and fiber profile shape intact. We attempted to avoid these complications through the use of dome flats, yet the intensity of the available dome lamps below ∼4000 Å is too low to determine an accurate fiber trace. Even if an acceptable light source was available, there is another issue with dome flats. It has been shown that the input acceptance angle is preserved through optical fibers and that focal ratio degradation is dependent on this angle (Carrasco & Parry 1994; Murphy et al. 2008). As light entering the fibers from a dome lamp is not collimated, there is a concern that the fiber cross-dispersion profile is not being properly quantified with the use of dome flats. Twilight flats avoid both of these issues.

Initially, the wavelength solution is estimated from unflattened arc frames. This can lead to errors in the wavelength solution when an arc line falls on top of a flat-field feature. Therefore, the determination of the wavelength solution and subsequent derivation of the flat-field frame is iterative. The arc lamp frames are flattened, and the wavelength solution is recalculated. As the flat-fielding procedure relies on the wavelength solution, a new flat field, based on the new wavelength solution, is also made. We find this iteration leaves the wavelength solution for most fibers unaffected, yet can improve the residuals by ∼0.05 Å for a handful of fibers where one or more of the arc lines used for the wavelength solution fall on strong flat-field features. A single iteration is all that is required.

The flat-field frame captures the pixel-to-pixel, fiber-to-fiber, and fiber profile shape variation for each fiber at very high S/N. However, due to thermal effects over an observing night, the science and sky frames can exhibit a shift in the position of the fiber profile. This shift manifests as a breathing mode and can reach up to a 0.3 pixel shift in the center of a fiber when the temperature gradient over the night is steep. A shift in the center of a fiber will lead to large flat-fielding errors if not accounted for. To correct for this effect, we have developed a heuristic solution. The general idea is to measure the offset over a subset of fibers, then create a unique flat for each science and sky frame based on the master flat for that night. We will refer to this frame as the *science flat* and it is generated as follows. For each fiber in each science frame, the difference between the fiber center of the master flat and science frame is calculated at all 2048 pixel positions. The median of these values for each fiber is taken, then smoothed with a 12 fiber-wide boxcar. As the breathing mode is smooth and continuous, and the signal in the science and sky frames can be quite low, this level of smoothing is both required and justified.

The fiber profiles have shapes that deviate slightly from any simple parameterization. For all resamplings, we employ a sinc interpolation, chosen for its non-parametric properties. Simply resampling each fiber's flat will properly capture the shift in fiber position, but will improperly capture the pixel-to-pixel features. Therefore, we run a 81 pixel-wide boxcar along the dispersion direction to isolate the fiber profile from the pixel-to-pixel variation. The original flat containing the proper pixel-to-pixel map and the resampled fiber profile are combined to form the final science flat. As sinc interpolation is not flux conserving, the science flat is renormalized to match the total counts in the original science frame. Once this unique flat is applied, we are left with science and sky frames that have been extracted, wavelength calibrated and flattened. The next step is sky subtraction.

A.2. Sky Subtraction

Figure 14 plots M87 spectra from three different spatial bins. An estimate of a typical night sky spectra is shown for comparison. The spectra are shown in CCD counts and the relative flux between the spectra has been preserved. At 1 R_e the galaxy is still brighter than the night sky by about a factor of two. By 2 R_e the night sky is now more than twice as bright as the galaxy, and in our furthest spatial bin the sky is ∼5 times brighter. A careful handling of sky subtraction at these low surface brightnesses is important, and we discuss our method in detail here. VIRUS-P does not have sky fibers and so sky nods are necessary. Lacking sky fibers has obvious drawbacks as we sample the sky at a different point in time, and loose science observing time to sky nods. Despite these disadvantages there are benefits to sky nods. One clear advantage to sky nods comes from the much improved noise statistics we get from sampling the sky with all 246 fibers. As our sky subtraction is done with a model of the night sky (described below) the addition of noise from the night sky estimate is reduced by $\sqrt{N}$, where N is the number of fibers. In contrast, Densepak and Sparsepak on the WIYN telescope dedicate 4.4% and 8.5% of their CCD to sky fibers, respectively (Barden & Wade 1988; Bershady et al. 2004) while the SAURON instrument dedicates just over 10% of its lenslets to estimates of the sky (Bacon et al. 2001). Sky nods also avoid the risk of cross-talk between the science and sky fibers, particularly when observing bright science targets.

A more serious issue with dedicated sky fibers is their limited offsets from the center of the science portion of the integral field unit. The sky fibers for Densepak and Sparsepak are offset 60″ and 70″ from the center of the science field. For SAURON this is increased to 154″ yet this size of offset can prove constraining for nearby galaxy work. For a galaxy like M87, whose half-light radius is ∼100″ and possibly larger (Kormendy et al. 2009), the

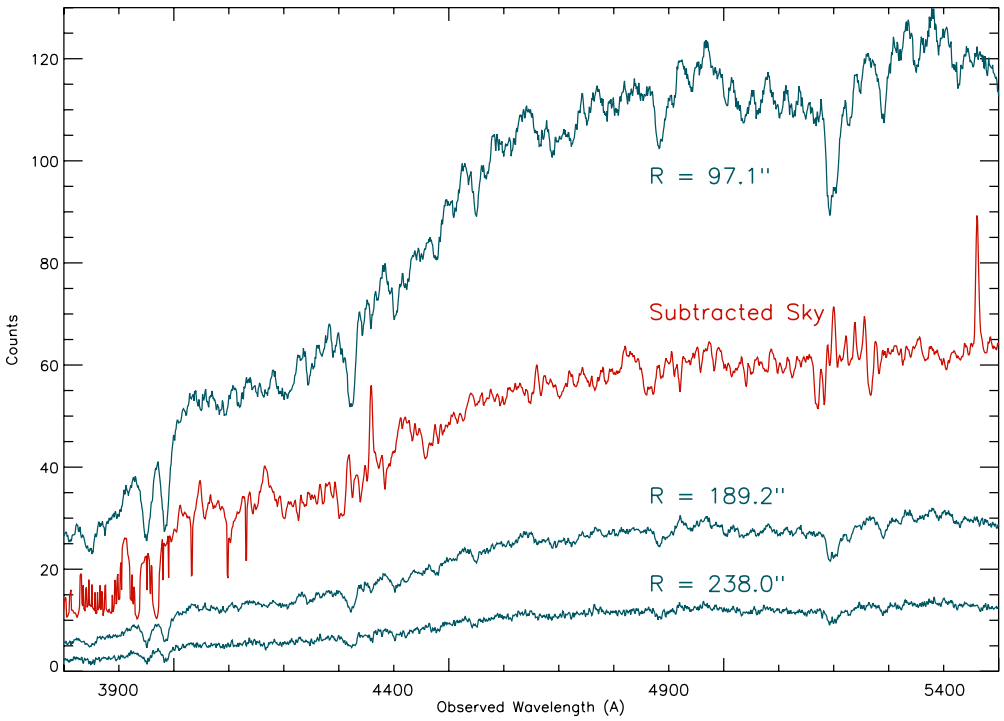

Figure 14. Spectra from three of the 88 spatial bins located at $R = 97.''1$, $189.''2$, and $238.''0$. The counts are a biweight combination of the CCD counts in ADU, after sky subtraction, over 20 fibers, 72 fibers, and 38 fibers, respectively. The typical level of the night sky is shown for comparison. The night sky subtracted from the most distant pointing at $R = 238''$ is ∼5 times brighter than the galaxy.

(A color version of this figure is available in the online journal.)

dedicated sky fibers are still collecting a significant amount of light from the galaxy itself, thus reducing the final S/N. It is clear that for M87, estimates of the sky at ∼150″ from the galaxy center will lead to subtraction of some level of galaxy light. How strong this effect is depends critically on how far out from the galaxy center the sky estimates come from.

With exposure times of 5 minutes for the sky nods and 20 minutes for the science frames, weights are given to the sky frames. The weighted sky frames are then summed to produce an estimate of the night sky. If the night sky did not evolve over 30 minutes, then the best sky estimate would come from weighting each neighboring sky nod by 2 and summing them. However, the sky can evolve on timescales less than 30 minutes. To account for this, 25 different sky estimates are made, each created by giving different weights to the neighboring sky nods. These frames are then sent through all of the reductions independently. Five different weights are used for each sky nod, ranging between 1.75 and 2.25 in 0.125 increments. With each sky nod receiving five different weights, the various combinations of sky nods lead to the $5^2 = 25$ estimates of the night sky. Once the remaining data reduction is complete we have 25 versions of each science frame. This range allows us to analyze, in a very direct way, both the best sky to subtract from each science frame, and the influence of our sky subtraction on the final stellar kinematics. We describe here how the individual sky frames are created from the sky nods and then discuss how the best sky to subtract from each science frame is selected from the 25 options.

For each of the 25 scaled sky frames bright continuum objects and cosmic rays are identified as 3σ outliers above the median and masked. As a 3σ cut may not catch low level sources, a 51 fiber-wide boxcar is run over the frame. A boxcar of this size corresponds to smoothing over a $107'' \times 21''$ region of the sky, so even faint, extended sources are removed. From this frame, the sky is modeled by the same method used to model the twilight sky during the creation of the flat field. The principle difference is that rather than modeling the sky to divide out of the frame, the sky model is what we are after.

The first step in determining the best level of sky to subtract is a visual inspection of the quality of subtraction of the night sky lines. However, the determination cannot be made based solely on these lines as they evolve on very short timescales and independently of the thermal background that most strongly effects our estimates of the stellar kinematics. The second step is to conduct a preliminary fit of a single template star (HD 20893) to the data. We outline the steps here, leaving the details of this fitting method to Section 3.1. First, for each of the 25 data frames, a set of fibers seeing a moderate level of galaxy light are selected and combined to form a single spectrum. The exact number of fibers and amount of galaxy light is not critical as the final determination comes from a relative comparison of the results. In fitting the data with a template star, a convolution occurs between the template star and an assumed line-of-sight velocity dispersion profile (LOSVD), which accounts for broadening in the spectra due to the temperature of the galaxy at that location. Normally, a continuum offset for the template star is allowed to float when conducting the extraction of kinematics. However, for this step, this value is fixed to avoid possible degeneracies between this parameter and the level of sky subtraction. A comparison of the residuals of the fit between each of the 25 frames and the single template star is used to determine the best level of sky subtraction. For nearly all frames (∼90%) the best sky subtraction comes from scaling each sky nod by 2 and summing them. The exception to this occurs primarily with exposures near dawn or dusk when twilight begins to affect the weighting.

As the sky evolves on timescales shorter than 30 minutes, the accuracy of our sky subtraction is not perfect and certain

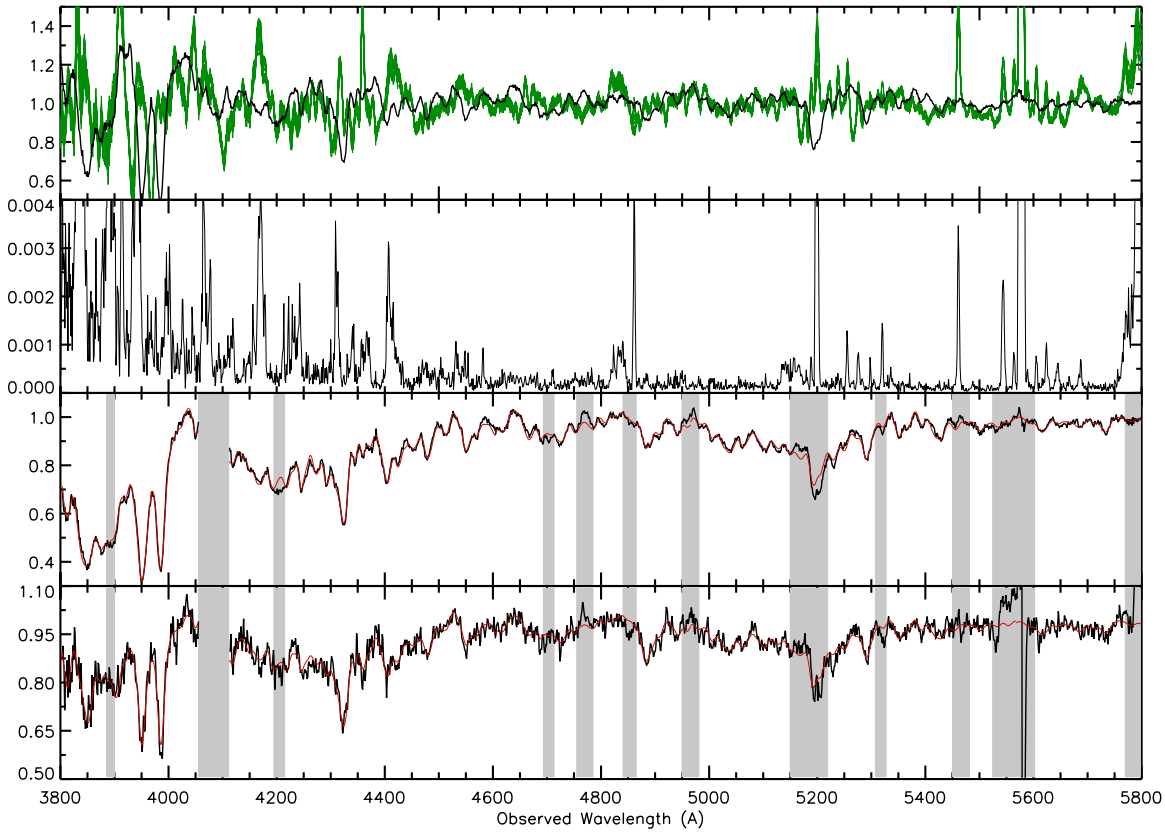

Figure 15. Top: the final VIRUS-P spectra for a spatial bin at $R = 60''$. The black spectra is the biweight combination of six fibers over 12 exposures. Overplotted in green are the 12 sky spectra subtracted from each exposure prior to the biweight combination. The continuum has been normalized here for plotting purposes. Middle top: the variance of the 12 sky spectra shown in the top panel. Note that while certain high variance regions are associated with night sky lines (e.g., 5200 Å), others are not associated with any strong night feature (e.g., 4860 Å). These variance plots are calculated for each spatial bin and used to help determine locations where the sky evolves on short timescales. Lower two panels: shown in black are the final spectra for two spatial bins at $R = 13.''2$ (upper) and $R = 222.''0$ (lower). Overplotted in red is the best-fit stellar template spectra. The gray areas in both lower figures indicate spectral regions that are suppressed when completing the kinematic extraction due to either issues with sky subtraction or template mismatch. We note that while these spectral regions are not fit when extracting the final stellar kinematics, the difference in the final LOSVD when the smaller regions ($\Delta\lambda \lesssim 50$ Å) are not masked is minimal. Table 2 shows how the spectra are split into five spectral regions prior to stellar template fitting.

(A color version of this figure is available in the online journal.)

spectral regions remain problematic, particularly around regions of bright sky emission lines. In order to get a handle on both the location and severity of these issues, we conduct a visual inspection of the data by overplotting the sky-subtracted galaxy spectra for a given spatial bin with each subtracted sky that goes into a given pointing. We show an example of the results of this inspection in Figure 15. In the top panel, the 12 different sky spectra subtracted from each 20 minute frame are overplotted on the resulting galaxy spectra. At each pixel, the variance is calculated for the 12 sky spectra and plotted in the second panel. A region of high variance indicates a region where the night sky evolves substantially between exposures. Notice that the high variance tends to be, but is not limited to, spectral regions with bright sky lines. The lower two panels in Figure 15 show the final sky subtracted spectra, along with the best-fit stellar template, for two spatial bins at $R = 13.''2$ and $222.''0$. The details of this fitting routine are given in Section 3.1. The gray areas indicate spectral regions excluded from the stellar template fitting. These regions are excluded when the template fit to the data is poor due to either issues with sky subtraction or template mismatch.

With 25 different estimates of the level of sky subtraction, we are in a good position to explore systematics due to either over or under subtracting the night sky. To do this, we select a range of spatial bins at various radii and S/N. We then take the reductions up through extraction of the LOSVD and compare the moments of the LOSVDs from the 25 frames. Although variation between these frames is seen, it is both random and within the uncertainties of our analysis. This is particularly true for central regions of the galaxy where our S/N is high. At larger radii, where the galaxy light is faint, over or under subtraction of the night sky tends to wash out the signal entirely rather than introduce systematics.

There is another component of the reductions that further mitigates error due to inaccurate sky subtraction. The final spectra is, at minimum, a combination of three separate frames, and up to 15 for the case of pointing 1. As the sky subtraction from each 20 minute exposure is independent, random poor sky subtraction is mitigated by having many frames. This mitigating effect gains strength for the more distant pointings, where the number of exposures increases.

A.3. Further Reductions

Once the sky subtraction is complete, cosmic rays are located and masked. To locate cosmic rays, each pixel value is compared to the pixel values that fall along either the same row or column of the extracted frame. Comparison with pixel values along the same row avoids masking continuum sources while comparison along the same column avoids masking real galaxy emission

features that will appear in neighboring fibers. A pixel found to be a 7σ outlier in this comparison is masked, as well as all neighboring pixels. Any low level cosmic rays not masked in this step are rejected when the spectra from different exposures and fibers is combined.

Next, fibers containing either foreground or background objects are located and masked. These fibers are identified by taking the median of the flux in each fiber and plotting these values against the position on the galaxy. As the median is taken over 5 rows $\times$ 2048 pixels = 10,240 values any residual cosmic rays or emission features will not influence this map. Foreground stars and background objects are located as outliers from the smooth continuum of the galaxy and masked. Although these objects will fall onto the same fibers for the same pointing, each science frame is inspected individually. We find this frame-by-frame check is necessary as transient objects, most notably satellites, can swamp an entire row of fibers.

Low level background sources remain a concern for the most distant pointings where the surface brightness of M87 may approach the level of these sources. As the final spectra for the most distant bins come from a biweight combination of between 30 and 70 fibers, and even a large background source will fall into just a few of our large fibers, any low level source will be rejected by the final biweight combination.

Each fiber for each night has a unique wavelength solution. Therefore, a linear interpolation is required before combining spectra from different fibers. The fiber cross-dispersion profile shape in each science frame is removed via division by the flat, and so the spectra from each of the five rows of a fiber is used in the biweight combination independently. In the case of pointing 3, where we have three science exposures, a minimum of 15 estimates of the spectra go into the biweight (1 fiber $\times$ 3 exposures $\times$ 5 rows). The biweight estimator has been shown to be robust for samples smaller than 15 (see Beers et al. 1990 for references). For our largest spatial bin, 72 fibers $\times$ 15 exposures $\times$ 5 rows = 5400 estimates are sent into the biweight. Once this step is complete we are left with the 88 VIRUS-P spectra presented in this work.

REFERENCES

Adams, J. J., Hill, G. J., & MacQueen, P. J. 2009, ApJ, 694, 314
Adams, J. J., et al. 2011, ApJS, in press (arXiv:1011.0426)
Avila, G. 1988, in ASP Conf. Ser. 3, Fiber Optics in Astronomy, ed. S. C. Barden (San Francisco, CA: ASP), 63
Bacon, R., et al. 2001, MNRAS, 326, 23
Barden, S. C., Elston, R., Armandroff, T., & Pryor, C. P. 1993, in ASP Conf. Ser. 37, Fiber Optics in Astronomy II, ed. P. M. Gray (San Francisco, CA: ASP), 223
Barden, S. C., & Wade, R. A. 1988, in ASP Conf. Ser. 3, Fiber Optics in Astronomy, ed. S. C. Barden (San Francisco, CA: ASP), 113
Barth, A. J., Ho, L. C., & Sargent, W. L. W. 2002, AJ, 124, 2607
Beers, T. C., Flynn, K., & Gebhardt, K. 1990, AJ, 100, 32
Bender, R., Saglia, R. P., & Gerhard, O. E. 1994, MNRAS, 269, 785
Bershady, M. A., Andersen, D. R., Harker, J., Ramsey, L. W., & Verheijen, M. A. W. 2004, PASP, 116, 565
Blanc, G. A., Heiderman, A., Gebhardt, K., Evans, N. J., & Adams, J. 2009, ApJ, 704, 842
Blanc, G. A., et al. 2010, ApJ, submitted (arXiv:1011.0430)
Bolton, A. S., Treu, T., Koopmans, L. V. E., Gavazzi, R., Moustakas, L. A., Burles, S., Schlegel, D. J., & Wayth, R. 2008, ApJ, 684, 248
Boylan-Kolchin, M., Springel, V., White, S. D. M., Jenkins, A., & Lemson, G. 2009, MNRAS, 398, 1150
Brandt, J. C., & Roosen, R. G. 1969, ApJ, 156, L59
Brighenti, F., & Mathews, W. G. 2001, ApJ, 553, 103
Cappellari, M., Verolme, E. K., van der Marel, R. P., Kleijn, G. A. V., Illingworth, G. D., Franx, M., Carollo, C. M., & de Zeeuw, P. T. 2002, ApJ, 578, 787
Cappellari, M., et al. 2006, MNRAS, 366, 1126
Carrasco, E., & Parry, I. R. 1994, MNRAS, 271, 1
Carrasco, E. R., et al. 2010, ApJ, 715, L160
Churazov, E., Forman, W., Vikhlinin, A., Tremaine, S., Gerhard, O., & Jones, C. 2008, MNRAS, 388, 1062
Churazov, E., et al. 2010, MNRAS, 404, 1165
Coccato, L., et al. 2009, MNRAS, 394, 1249
Cohen, J. G. 2000, AJ, 119, 162
Cohen, J. G., & Ryzhov, A. 1997, ApJ, 486, 230
Colless, M., et al. 2001, MNRAS, 328, 1039
Copin, Y., Cretton, N., & Emsellem, E. 2004, A&A, 415, 889
Côté, P., et al. 2001, ApJ, 559, 828
Craig, W. W., Hailey, C. J., & Brodie, J. P. 1988, in ASP Conf. Ser. 3, Fiber Optics in Astronomy, ed. S. C. Barden (San Francisco, CA: ASP), 41
Cretton, N., de Zeeuw, P. T., van der Marel, R. P., & Rix, H. 1999, ApJS, 124, 383
Cretton, N., Rix, H., & de Zeeuw, P. T. 2000, ApJ, 536, 319
Das, P., Gerhard, O., Churazov, E., & Zhuravleva, I. 2010, MNRAS, 409, 1362
Davis, M., Efstathiou, G., Frenk, C. S., & White, S. D. 1985, ApJ, 292, 371
Davis, M., Huchra, J., Latham, D. W., & Tonry, J. 1982, ApJ, 253, 423
Dejonghe, H., & Merritt, D. 1992, ApJ, 391, 531
Dierckx, P. 1993, Curve and Surface Fitting with Splines (New York: Oxford Clarendon)
Doherty, M., et al. 2009, A&A, 502, 771
Donato, F., et al. 2009, MNRAS, 397, 1169
Douglas, N. G., et al. 2007, ApJ, 664, 257
Dressler, A., Lynden-Bell, D., Burstein, D., Davies, R. L., Faber, S. M., Terlevich, R., & Wegner, G. 1987, ApJ, 313, 42
Dressler, A., & Richstone, D. O. 1988, ApJ, 324, 701
Dubinski, J., & Carlberg, R. G. 1991, ApJ, 378, 496
Einasto, J. 1965, Trudy Inst. Astrofiz. Alma-Ata, 5, 87
Einasto, J. 1968, Tartu Astron. Obs. Publ., 36, 414
Emsellem, E., et al. 2004, MNRAS, 352, 721
Fabricant, D., & Gorenstein, P. 1983, ApJ, 267, 535
Fillmore, J. A., & Goldreich, P. 1984, ApJ, 281, 1
Forestell, A. D. 2009, PhD thesis, Univ. Texas at Austin
Forestell, A. D., & Gebhardt, K. 2010, ApJ, 716, 370
Frenk, C. S., White, S. D. M., Efstathiou, G., & Davis, M. 1985, Nature, 317, 595
Gebhardt, K., Adams, J., Richstone, D., Lauer, T. R., Faber, S. M., Gultekin, K., Murphy, J., & Tremaine, S. 2011, arXiv:1101.1954
Gebhardt, K., & Thomas, J. 2009, ApJ, 700, 1690
Gebhardt, K., et al. 1996, AJ, 112, 105
Gebhardt, K., et al. 2000, AJ, 119, 1157
Gebhardt, K., et al. 2003, ApJ, 583, 92
Gerhard, O. E. 1993, MNRAS, 265, 213
Gerhard, O., Kronawitter, A., Saglia, R. P., & Bender, R. 2001, AJ, 121, 1936
Ghigna, S., Moore, B., Governato, F., Lake, G., Quinn, T., & Stadel, J. 2000, ApJ, 544, 616
Graves, G. J., & Faber, S. M. 2010, ApJ, 717, 803
Graves, G. J., & Schiavon, R. P. 2008, ApJS, 177, 446
Gunn, J. E., & Gott, J. R., III 1972, ApJ, 176, 1
Hanes, D. A., Côté, P., Bridges, T. J., McLaughlin, D. E., Geisler, D., Harris, G. L. H., Hesser, J. E., & Lee, M. G. 2001, ApJ, 559, 812
Hill, G. J., et al. 2006, Proc. SPIE, 6269, 62692J-1
Hill, G. J., et al. 2008a, in ASP Conf. Ser. 399, ed. T. Kodama, T. Yamada, & K. Aoki (San Francisco, CA: ASP), 115
Hill, G. J., et al. 2008b, Proc. SPIE, 7014, 115
Hoffman, L., Cox, T. J., Dutta, S., & Hernquist, L. 2010, ApJ, 723, 818
Huchra, J., & Brodie, J. 1987, AJ, 93, 779
Humphrey, P. J., Buote, D. A., Gastaldello, F., Zappacosta, L., Bullock, J. S., Brighenti, F., & Mathews, W. G. 2006, ApJ, 646, 899
Jimenez, R., Verde, L., & Oh, S. P. 2003, MNRAS, 339, 243
Keeton, C. R. 2001, ApJ, 561, 46
Kelson, D. D. 2003, PASP, 115, 688
Kormendy, J., Fisher, D. B., Cornell, M. E., & Bender, R. 2009, ApJS, 182, 216
Krajnović, D., Cappellari, M., Emsellem, E., McDermid, R. M., & de Zeeuw, P. T. 2005, MNRAS, 357, 1113
Kuntschner, H., Lucey, J. R., Smith, R. J., Hudson, M. J., & Davies, R. L. 2001, MNRAS, 323, 615
Lauer, T. R., et al. 1992, AJ, 103, 703
Lissandrini, C., Cristiani, S., & La Franca, F. 1994, PASP, 106, 1157
Lynden-Bell, D. 1967, MNRAS, 136, 101
Magorrian, J. 1999, MNRAS, 302, 530
Mandelbaum, R., Seljak, U., Kauffmann, G., Hirata, C. M., & Brinkmann, J. 2006, MNRAS, 368, 715
Matsushita, K., Belsole, E., Finoguenov, A., & Böhringer, H. 2002, A&A, 386, 77

McLaughlin, D. E. 1999, AJ, 117, 2398
Merritt, D., & Tremblay, B. 1993, AJ, 106, 2229
Mihos, J. C., Harding, P., Feldmeier, J., & Morrison, H. 2005, ApJ, 631, L41
Moni Bidin, C., Carraro, G., Méndez, R. A., & van Altena, W. F. 2010, ApJ, 724, L122
Moore, B., Governato, F., Quinn, T., Stadel, J., & Lake, G. 1998a, ApJ, 499, L5
Moore, B., Governato, F., Quinn, T., Stadel, J., & Lake, G. 1998b, ApJ, 499, L5
Mould, J. R., Oke, J. B., & Nemec, J. M. 1987, AJ, 93, 53
Murphy, J. D., MacQueen, P. J., Hill, G. J., Grupp, F., Kelz, A., Paulunas, P., Roth, M. M., & Fry, A. 2008, Proc. SPIE, 7014, 70182T-1
Navarro, J. F., Frenk, C. S., & White, S. D. 1995, MNRAS, 275, 56
Navarro, J. F., Frenk, C. S., & White, S. D. 1997, ApJ, 490, 493
Navarro, J. F., Frenk, C. S., & White, S. D. M. 1996, ApJ, 462, 563
Nieto, J., & Monnet, G. 1984, A&A, 139, 464
Parry, I. R., & Carrasco, E. 1990, Proc. SPIE, 1235, 702
Pinkney, J., et al. 2003, ApJ, 596, 903
Poveda, A. 1961, ApJ, 134, 910
Press, W. H., & Schechter, P. 1974, ApJ, 187, 425
Ramsey, L. W. 1988, in ASP Conf. Ser. 3, Fiber Optics in Astronomy, ed. S. C. Barden (San Francisco, CA: ASP), 26
Rix, H.-W., de Zeeuw, P. T., Cretton, N., van der Marel, R. P., & Carollo, C. M. 1997, ApJ, 488, 702
Romanowsky, A. J., Douglas, N. G., Arnaboldi, M., Kuijken, K., Merrifield, M. R., Napolitano, N. R., Capaccioli, M., & Freeman, K. C. 2003, Science, 301, 1696
Romanowsky, A. J., & Kochanek, C. S. 2001, ApJ, 553, 722
Romanowsky, A. J., Strader, J., Spitler, L. R., Johnson, R., Brodie, J. P., Forbes, D. A., & Ponman, T. 2009, AJ, 137, 4956
Rubin, V. C., Ford, W. K. J., & Thonnard, N. 1980, ApJ, 238, 471
Sánchez, S. F. 2006, Astron. Nachr., 327, 850
Sánchez-Blázquez, P., et al. 2006, MNRAS, 371, 703
Sand, D. J., Treu, T., Ellis, R. S., Smith, G. P., & Kneib, J. 2008, ApJ, 674, 711
Sandin, C., Becker, T., Roth, M. M., Gerssen, J., Monreal-Ibero, A., Böhm, P., & Weilbacher, P. 2010, A&A, 515, A35
Sargent, W. L. W., Young, P. J., Lynds, C. R., Boksenberg, A., Shortridge, K., & Hartwick, F. D. A. 1978, ApJ, 221, 731
Schmoll, J., Roth, M. M., & Laux, U. 2003, PASP, 115, 854
Schwarzschild, M. 1979, ApJ, 232, 236
Sembach, K. R., & Tonry, J. L. 1996, AJ, 112, 797
Sersic, J. L. 1968, Atlas de Galaxias australes (Cordoba: Observatorio Astronomico, Universidad Nacional de Cordoba)
Shen, J., & Gebhardt, K. 2010, ApJ, 711, 484
Siopis, C., et al. 2009, ApJ, 693, 946
Sofue, Y., & Rubin, V. 2001, ARA&A, 39, 137
Springel, V., et al. 2005, Nature, 435, 629
Springel, V., et al. 2008, MNRAS, 391, 1685
Terlevich, R., Davies, R. L., Faber, S. M., & Burstein, D. 1981, MNRAS, 196, 381
Thomas, J., Saglia, R. P., Bender, R., Thomas, D., Gebhardt, K., Magorrian, J., Corsini, E. M., & Wegner, G. 2005, MNRAS, 360, 1355
Thomas, J., Saglia, R. P., Bender, R., Thomas, D., Gebhardt, K., Magorrian, J., Corsini, E. M., & Wegner, G. 2007, MNRAS, 382, 657
Thomas, J., Saglia, R. P., Bender, R., Thomas, D., Gebhardt, K., Magorrian, J., & Richstone, D. 2004, MNRAS, 353, 391
Treu, T., & Koopmans, L. V. E. 2004, ApJ, 611, 739
Tsai, J. C. 1996, in ASP Conf. Ser. 88, Clusters, Lensing, and the Future of the Universe, ed. V. Trimble & A. Reisenegger (San Francisco, CA: ASP), 275
Turner, J. E. H., Miller, B. W., Beck, T. L., Song, I., Cooke, A. J., Seaman, R. L., & Valdés, F. G. 2006, New Astron. Rev., 49, 655
Valdes, F., Gupta, R., Rose, J. A., Singh, H. P., & Bell, D. J. 2004, ApJS, 152, 251
Valluri, M., Vass, I. M., Kazantzidis, S., Kravtsov, A. V., & Bohn, C. L. 2007, ApJ, 658, 731
van Albada, T. S., & Sancisi, R. 1986, Phil. Trans. R. Soc., 320, 447
van den Bosch, R. C. E., van de Ven, G., Verolme, E. K., Cappellari, M., & de Zeeuw, P. T. 2008, MNRAS, 385, 647
van der Marel, R. P. 1994, MNRAS, 270, 271
van der Marel, R. P., Cretton, N., de Zeeuw, P. T., & Rix, H. 1998, ApJ, 493, 613
Verolme, E. K., & de Zeeuw, P. T. 2002, MNRAS, 331, 959
Watson, F., Offer, A. R., Lewis, I. J., Bailey, J. A., & Glazebrook, K. 1998, in ASP Conf. Ser. 152, Fiber Optics in Astronomy III, ed. S. Arribas, E. Mediavilla, & F. Watson (San Francisco, CA: ASP), 50
Weijmans, A., et al. 2009, MNRAS, 398, 561
White, S., & Rees, M. 1978, MNRAS, 183, 341
Worthey, G., Faber, S. M., & Gonzalez, J. J. 1992, ApJ, 398, 69
Wu, X., & Tremaine, S. 2006, ApJ, 643, 210
Wyse, R. F. G., & Gilmore, G. 1992, MNRAS, 257, 1
Yoachim, P., Roskar, R., & Debattista, V. P. 2009, BAAS, 41, 326
Yoachim, P., Roškar, R., & Debattista, V. P. 2010, ApJ, 716, L4
Young, P. J., Westphal, J. A., Kristian, J., Wilson, C. P., & Landauer, F. P. 1978, ApJ, 221, 721
Zanichelli, A., et al. 2005, PASP, 117, 1271